Thermochemical Non-Equilibrium Reentry Flows in Three-Dimensions – Part I – Structured Solutions

EDISSON SÁVIO DE GÓES MACIEL[(1)] and AMILCAR PORTO PIMENTA[(2)]
Aeronautical Engineering Division (IEA)
ITA – Aeronautical Technological Institute
Praça Mal. do Ar Eduardo Gomes, 50 – Vila das Acácias – São José dos Campos – SP – 12228-900
BRAZIL
[(1)]edisavio@edissonsavio.eng.br; [(1)]http://edissonsavio.eng.br and [(2)]amilcar@ita.br

Abstract: - This work presents a numerical tool implemented to simulate inviscid and viscous flows employing the reactive gas formulation of thermal and chemical non-equilibrium. The Euler and Navier-Stokes equations, employing a finite volume formulation, on the context of structured and unstructured spatial discretizations, are solved. These variants allow an effective comparison between the two types of spatial discretization aiming verify their potentialities: solution quality, convergence speed, computational cost, etc. The aerospace problem involving the hypersonic "hot gas" flow around a blunt body, in three-dimensions, is simulated. The reactive simulations will involve an air chemical model of five species: N, O, N_2, O_2 and NO. Seventeen chemical reactions, involving dissociation and recombination, will be simulated by the proposed model. The Arrhenius formula will be employed to determine the reaction rates and the law of mass action will be used to determine the source terms of each gas species equation. In this first part, only the structured solutions are presented. The unstructured solutions are shown in the second part of this study.

Key-Words: - Thermochemical non-equilibrium, Reentry flow, Five species chemical model, Arrhenius formula, Structured and unstructured solutions, Euler and Navier-Stokes equations, Three-Dimensions.

1 Introduction

The study of hypersonic flows has gained momentum with the advent of concepts like the National AeroSpace Plane (NASP) and similar transatmospheric vehicles. Under the very high velocity and temperature conditions experienced by hypersonic vehicles, departure from chemical and thermal equilibrium occurs. Properties of air change dramatically as new chemical species are produced at the expense of others. The simple one temperature model used to describe the energy of air becomes inapplicable, and it becomes necessary to consider one or more additional temperatures (corresponding to vibrational and electronic energies). Determination of aerothermal loads on blunt bodies in such an environment is of great importance.

In high speed flows, any adjustment of chemical composition or thermodynamic equilibrium to a change in local environment requires certain time. This is because the redistribution of chemical species and internal energies require certain number of molecular collisions, and hence a certain characteristic time. Chemical non-equilibrium occurs when the characteristic time for the chemical reactions to reach local equilibrium is of the same order as the characteristic time of the fluid flow. Similarly, thermal non-equilibrium occurs when the characteristic time for translation and various internal energy modes to reach local equilibrium is of the same order as the characteristic time of the fluid flow. Since chemical and thermal changes are the results of collisions between the constituent particles, non-equilibrium effects prevail in high-speed flows in low-density air.

In chemical non-equilibrium flows the mass conservation equation is applied to each of the constituent species in the gas mixture. Therefore, the overall mass conservation equation is replaced by as many species conservation equations as the number of chemical species considered. The assumption of thermal non-equilibrium introduces additional energy conservation equations – one for every additional energy mode. Thus, the number of governing equations for non-equilibrium flow is much bigger compared to those for perfect gas flow. A complete set of governing equations for non-equilibrium flow may be found in [1-2].

Analysis of non-equilibrium flow is rather complex because (1) the number of equations to be solved is much larger than the Navier-Stokes equations, and (2) there are additional terms like the species production, mass diffusion, and vibrational energy relaxation, etc., that appear in the governing equations. In a typical flight of the NASP flying at Mach 15, ionization is not expected to occur, and a

5-species air is adequate for the analysis (see [3]). Since the rotational characteristic temperatures for the constituent species (namely N, O, N_2, O_2 and NO) are small, the translational and rotational energy modes are assumed to be in equilibrium, whereas the vibrational energy mode is assumed to be in non-equilibrium. [4] has simplified the thermodynamic model by assuming a harmonic oscillator to describe the vibrational energy. Ionic species and electrons are not considered. This simplifies the set of governing equations by eliminating the equation governing electron and electronic excitation energy. [4] has taken the complete set of governing equations from [1], and simplified them for a five-species two-temperature air model.

The problems of chemical non-equilibrium in the shock layers over vehicles flying at high speeds and high altitudes in the Earth's atmosphere have been discussed by several investigators ([5-8]). Most of the existing computer codes for calculating the non-equilibrium reacting flow use the one-temperature model, which assumes that all of the internal energy modes of the gaseous species are in equilibrium with the translational mode ([7-8]). It has been pointed out that such a one-temperature description of the flow leads to a substantial overestimation of the rate of equilibrium because of the elevated vibrational temperature [6]. A three-temperature chemical-kinetic model has been proposed by [9] to describe the relaxation phenomena correctly in such a flight regime. However, the model is quite complex and requires many chemical rate parameters which are not yet known. As a compromise between the three-temperature and the conventional one-temperature model, a two-temperature chemical-kinetic model has been developed ([10-11]), which is designated herein as the TT_v model. The TT_v model uses one temperature T to characterize both the translational energy of the atoms and molecules and the rotational energy of the molecules, and another temperature T_v to characterize the vibrational energy of the molecules, translational energy of the electrons, and electronic excitation energy of atoms and molecules. The model has been applied to compute the thermodynamic properties behind a normal shock wave in a flow through a constant-area duct ([10-11]). Radiation emission from the non-equilibrium flow has been calculated using the Non-equilibrium Air Radiation (NEQAIR) program ([12-13]). The flow and the radiation computations have been packaged into a single computer program, the Shock-Tube Radiation Program (STRAP) ([11]).

A first-step assessment of the TT_v model was made in [11] where it was used in computing the flow properties and radiation emission from the flow in a shock tube for pure nitrogen undergoing dissociation and weak ionization (ionization fraction less than 0.1%). Generally good agreement was found between the calculated radiation emission and those obtained experimentally in shock tubes ([14-16]). The only exception involved the vibrational temperature. The theoretical treatment of the vibrational temperature could not be validated because the existing data on the vibrational temperature behind a normal shock wave ([16]) are those for an electronically excited state of the molecular nitrogen ion N_2^+ instead of the ground electronic state of the neutral nitrogen molecule N_2 which is calculated in the theoretical model. The measured vibrational temperature of N_2^+ was much smaller than the calculated vibrational temperature for N_2.

This work, first part of this study, describes a numerical tool to perform thermochemical non-equilibrium simulations of reactive flow in three-dimensions. The [17] scheme, in its first- and second-order versions, is implemented to accomplish the numerical simulations. The Euler and Navier-Stokes equations, on a finite volume context and employing structured and unstructured spatial discretizations, are applied to solve the "hot gas" hypersonic flow around a blunt body in three-dimensions. The second-order version of the [17] scheme is obtained from a "MUSCL" extrapolation procedure in a context of structured spatial discretization. In the unstructured context, only first-order solutions are obtained. The convergence process is accelerated to the steady state condition through a spatially variable time step procedure, which has proved effective gains in terms of computational acceleration (see [18-19]).

The reactive simulations involve an air chemical model of five species: N, O, N_2, O_2 and NO. Seventeen chemical reactions, involving dissociation and recombination, are simulated by the proposed model. The Arrhenius formula is employed to determine the reaction rates and the law of mass action is used to determine the source terms of each gas species equation.

The results have demonstrated that the most correct value of the stagnation pressure is obtained by the [17] scheme, in its first order and viscous structured case, with an error of 5.08%. Moreover, the best value to the shock stand-off distance is estimated by the [17] scheme, second order and viscous structured case, with an error of 5.26%. In qualitative terms, the second order versions of the

thermal equilibrium and chemical non-equilibrium as well the thermochemical non-equilibrium algorithms predict closest shock waves to the blunt nose than their first order counterpart.

2 Formulation to Reactive Flow in Thermochemical Non-Equilibrium

2.1 Reactive Equations in Three-Dimensions

The reactive Navier-Stokes equations in thermal and chemical non-equilibrium were implemented on a finite volume context, in the three-dimensional space. In this case, these equations in integral and conservative forms can be expressed by:

$$\frac{\partial}{\partial t}\int_V Q dV + \int_S \vec{F}\bullet\vec{n} dS = \int_V S_{CV} dV \text{, with}$$

$$\vec{F} = (E_e - E_v)\vec{i} + (F_e - F_v)\vec{j} + (G_e - G_v)\vec{k}, \quad (1)$$

where: Q is the vector of conserved variables, V is the volume of a computational cell, $\vec{F}$ is the complete flux vector, $\vec{n}$ is the unity vector normal to the flux face, S is the flux area, S_{CV} is the chemical and vibrational source term, E_e, F_e and G_e are the convective flux vectors or the Euler flux vectors in the x, y and z directions, respectively, E_v, F_v and G_v are the viscous flux vectors in the x, y and z directions, respectively. The $\vec{i}$, $\vec{j}$ and $\vec{k}$ unity vectors define the Cartesian coordinate system. Ten (10) conservation equations are solved: one of general mass conservation, three of linear momentum conservation, one of total energy, four of species mass conservation and one of the vibrational internal energy of the molecules. Therefore, one of the species is absent of the iterative process. The CFD ("Computational Fluid Dynamics") literature recommends that the species of biggest mass fraction of the gaseous mixture should be omitted, aiming to result in a minor numerical accumulation error, corresponding to the biggest mixture constituent (in the case, the air). To the present study, in which is chosen a chemical model to the air composed of five (5) chemical species (N, O, N_2, O_2 and NO) and seventeen (17) chemical reactions, being fifteen (15) dissociation reactions (endothermic reactions) and two (2) of exchange or recombination, this species can be the N_2 or the O_2. To this work, it was chosen the N_2. The vectors Q, E_e, F_e, G_e, E_v, F_v, G_v and S_{CV} can, hence, be defined as follows ([4]):

$$Q = \begin{Bmatrix} \rho \\ \rho u \\ \rho v \\ \rho w \\ e \\ \rho_1 \\ \rho_2 \\ \rho_4 \\ \rho_5 \\ \rho e_V \end{Bmatrix}, \quad E_e = \begin{Bmatrix} \rho u \\ \rho u^2 + p \\ \rho uv \\ \rho uw \\ \rho Hu \\ \rho_1 u \\ \rho_2 u \\ \rho_4 u \\ \rho_5 u \\ \rho e_V u \end{Bmatrix}; \quad (2)$$

$$F_e = \begin{Bmatrix} \rho v \\ \rho vu \\ \rho v^2 + p \\ \rho vw \\ \rho Hv \\ \rho_1 v \\ \rho_2 v \\ \rho_4 v \\ \rho_5 v \\ \rho e_V v \end{Bmatrix}, \quad G_e = \begin{Bmatrix} \rho w \\ \rho wu \\ \rho wv \\ \rho w^2 + p \\ \rho Hw \\ \rho_1 w \\ \rho_2 w \\ \rho_4 w \\ \rho_5 w \\ \rho e_V w \end{Bmatrix}; \quad (3)$$

$$E_v = \frac{1}{Re}\begin{Bmatrix} 0 \\ \tau_{xx} \\ \tau_{xy} \\ \tau_{xz} \\ \tau_{xx}u + \tau_{xy}v + \tau_{xz}w - q_{f,x} - q_{v,x} - \phi_x \\ -\rho_1 v_{1x} \\ -\rho_2 v_{2x} \\ -\rho_4 v_{4x} \\ -\rho_5 v_{5x} \\ -q_{v,x} - \phi_{v,x} \end{Bmatrix}; \quad (4)$$

in which: ρ is the mixture density; u, v and w are Cartesian components of the velocity vector in the x, y and z directions, respectively; p is the fluid static pressure; e is the fluid total energy; ρ_1, ρ_2, ρ_4 and ρ_5 are densities of the N, O, O_2 and NO, respectively; H is the mixture total enthalpy; e_V is the sum of the vibrational energy of the molecules; the τ's are the components of the viscous stress tensor; $q_{f,x}$, $q_{f,y}$ and $q_{f,z}$ are the frozen components of

the Fourier-heat-flux vector in the x, y and z directions, respectively;

$$F_v = \frac{1}{Re}\begin{Bmatrix} 0 \\ \tau_{xy} \\ \tau_{yy} \\ \tau_{yz} \\ \tau_{xy}u + \tau_{yy}v + \tau_{yz}w - q_{f,y} - q_{v,y} - \phi_y \\ -\rho_1 v_{1y} \\ -\rho_2 v_{2y} \\ -\rho_4 v_{4y} \\ -\rho_5 v_{5y} \\ -q_{v,y} - \phi_{v,y} \end{Bmatrix}; \quad (5)$$

$$G_v = \frac{1}{Re}\begin{Bmatrix} 0 \\ \tau_{zx} \\ \tau_{zy} \\ \tau_{zz} \\ \tau_{zx}u + \tau_{zy}v + \tau_{zz}w - q_{f,z} - q_{v,z} - \phi_z \\ -\rho_1 v_{1z} \\ -\rho_2 v_{2z} \\ -\rho_4 v_{4z} \\ -\rho_5 v_{5z} \\ -q_{v,z} - \phi_{v,z} \end{Bmatrix}; \quad (6)$$

$$S_{CV} = \begin{Bmatrix} 0 \\ 0 \\ 0 \\ 0 \\ 0 \\ \dot{\omega}_1 \\ \dot{\omega}_2 \\ \dot{\omega}_4 \\ \dot{\omega}_5 \\ \sum_{s=mol} \rho_s \left(e^*_{v,s} - e_{v,s}\right)/\tau_s + \sum_{s=mol} \dot{\omega}_s e_{v,s} \end{Bmatrix}, \quad (7)$$

$q_{v,x}$, $q_{v,y}$ and $q_{v,z}$ are the components of the Fourier-heat-flux vector calculated with the vibrational thermal conductivity and vibrational temperature; $\rho_s v_{sx}$, $\rho_s v_{sy}$ and $\rho_s v_{sz}$ represent the species diffusion flux, defined by the Fick law; ϕ_x, ϕ_y and ϕ_z are the terms of mixture diffusion; $\phi_{v,x}$, $\phi_{v,y}$ and $\phi_{v,z}$ are the terms of molecular diffusion calculated at the vibrational temperature; $\dot{\omega}_s$ is the chemical source term of each species equation, defined by the law of mass action; e^*_v is the molecular-vibrational-internal energy calculated with the translational/rotational temperature; and τ_s is the translational-vibrational characteristic relaxation time of each molecule.

The viscous stresses, in N/m^2, are determined, according to a Newtonian fluid model, by:

$$\tau_{xx} = 2\mu\frac{\partial u}{\partial x} - \frac{2}{3}\mu\left(\frac{\partial u}{\partial x} + \frac{\partial v}{\partial y} + \frac{\partial w}{\partial z}\right); \quad (8)$$

$$\tau_{xy} = \mu\left(\frac{\partial u}{\partial y} + \frac{\partial v}{\partial x}\right), \quad \tau_{xz} = \mu\left(\frac{\partial u}{\partial z} + \frac{\partial w}{\partial x}\right); \quad (9)$$

$$\tau_{yy} = 2\mu\frac{\partial v}{\partial y} - \frac{2}{3}\mu\left(\frac{\partial u}{\partial x} + \frac{\partial v}{\partial y} + \frac{\partial w}{\partial z}\right); \quad (10)$$

$$\tau_{yz} = \mu\left(\frac{\partial v}{\partial z} + \frac{\partial w}{\partial y}\right); \quad (11)$$

$$\tau_{zz} = 2\mu\frac{\partial w}{\partial z} - \frac{2}{3}\mu\left(\frac{\partial u}{\partial x} + \frac{\partial v}{\partial y} + \frac{\partial w}{\partial z}\right), \quad (12)$$

in which μ is the fluid molecular viscosity.

The frozen components of the Fourier-heat-flux vector, which considers only thermal conduction, are defined by:

$$q_{f,x} = -k_f\frac{\partial T}{\partial x},\ q_{f,y} = -k_f\frac{\partial T}{\partial y} \text{ and } q_{f,z} = -k_f\frac{\partial T}{\partial z} \quad (13)$$

where k_f is the mixture frozen thermal conductivity, calculated conform presented in subsection **2.3.4.** The vibrational components of the Fourier-heat-flux vector are calculated as follows:

$$q_{v,x} = -k_v\frac{\partial T_v}{\partial x},\ q_{v,y} = -k_v\frac{\partial T_v}{\partial y} \text{ and } q_{v,z} = -k_v\frac{\partial T_v}{\partial z}, \quad (14)$$

in which k_v is the vibrational thermal conductivity and T_v is the vibrational temperature, what characterizes this model as of two temperatures: translational/rotational and vibrational. The calculation of T_v and k_v are demonstrated in subsections **2.2.2** and **2.3.4**, respectively.

The terms of species diffusion, defined by the Fick law, to a condition of thermal non-equilibrium, are determined by ([4]):

$$\rho_s v_{sx} = -\rho D_s \frac{\partial Y_{MF,s}}{\partial x}, \quad \rho_s v_{sy} = -\rho D_s \frac{\partial Y_{MF,s}}{\partial y};$$

$$\rho_s v_{sz} = -\rho D_s \frac{\partial Y_{MF,s}}{\partial z} \qquad (15)$$

with "s" referent to a given species, $Y_{MF,s}$ being the molar fraction of the species, defined as:

$$Y_{MF,s} = \frac{\rho_s / M_s}{\sum_{k=1}^{ns} \rho_k / M_k} \qquad (16)$$

and D_s is the species-effective-diffusion coefficient.

The diffusion terms ϕ_x, ϕ_y and ϕ_z which appear in the energy equation are defined by ([20]):

$$\phi_x = \sum_{s=1}^{ns} \rho_s v_{sx} h_s, \quad \phi_y = \sum_{s=1}^{ns} \rho_s v_{sy} h_s;$$

$$\phi_z = \sum_{s=1}^{ns} \rho_s v_{sz} h_s, \qquad (17)$$

being h_s the specific enthalpy (sensible) of the chemical species "s". Details of the calculation of the specific enthalpy, see [21-22]. The molecular diffusion terms calculated at the vibrational temperature, $\phi_{v,x}$, $\phi_{v,y}$ and $\phi_{v,z}$, which appear in the vibrational-internal-energy equation are defined by ([4]):

$$\phi_{v,x} = \sum_{s=mol} \rho_s v_{sx} h_{v,s}, \ \phi_{v,y} = \sum_{s=mol} \rho_s v_{sy} h_{v,s};$$

$$\phi_{v,z} = \sum_{s=mol} \rho_s v_{sz} h_{v,s}, \qquad (18)$$

with $h_{v,s}$ being the specific enthalpy (sensible) of the chemical species "s" calculated at the vibrational temperature T_v. The sum of Eq. (18), as also those present in Eq. (7), considers only the molecules of the system, namely: N_2, O_2 and NO.

2.2 Thermodynamic Model/Thermodynamic Properties

2.2.1 Definition of general parameters

$$p = RT\sum_{s=1}^{ns} \rho_s / M_s = \rho\sigma RT \therefore \rho\sigma = \sum_{s=1}^{ns} \rho_s / M_s = \rho \sum_{s=1}^{ns} c_s / M_s \Rightarrow$$

$$\sigma = \sum_{s=1}^{ns} c_s / M_s, \qquad (19)$$

in which: σ is the mixture number in kg-mol/kg and c_s is the mass fraction (non-dimensional), defined by $c_s = \rho_s / \rho$.

$$\sigma = \sum_{s=1}^{ns} \sigma_s \Rightarrow \sigma_s = c_s / M_s;$$

$$M_{mixt} = 1/\sigma \therefore M_{mixt} = 1 \Big/ \sum_{s=1}^{ns} c_s / M_s;$$

$$e^*_{v,s} = e_{v,s}(T_v = T), \qquad (20)$$

with: σ_s being the number of kg-mol/kg of species "s" and M_{mixt} is the mixture molecular mass, in kg/kg-mol.

2.2.2 Thermodynamic model

(a) Mixture translational internal energy:

$$e_T = \sum_{s=1}^{ns} e_{T,s}\sigma_s = \sum_{s=1}^{ns} \left[\int_0^T C_{v,T,s}(T')dT' + h^0 \right] \sigma_s, \qquad (21)$$

where: $e_{T,s}$ is the translational internal energy per kg-mol of species "s", in J/kg-mol. The specific heat at constant volume per kg-mol of species "s" due to translation, in J/(kg-mol.K), is defined by:

$$C_{v,T,s}(T) = 1.5R. \qquad (22)$$

Hence,

$$e_{T,s}(T) = 1.5RT + h^0 \Rightarrow e_T(T) = \sum_{s=1}^{ns} \sigma_s \left(1.5RT + h^0\right) \qquad (23)$$

with: e_T being the translational internal energy per unity of the gaseous mixture mass, in J/kg, and h^0 being the formation enthalpy of the species "s" per kg-mol of species, J/kg-mol. It is important to note that:

$$e_T(T) = \sum_{s=1}^{ns} \sigma_s \left(1.5RT + h^0\right) = \sum_{s=1}^{ns} c_s \left(1.5\frac{R}{M_s}T + \frac{h^0}{M_s}\right) =$$

$$\sum_{s=1}^{ns} c_s \left(1.5R_s T + h_s^0\right) \Rightarrow e_T(T) = \sum_{s=1}^{ns} c_s \left(1.5R_s T + h_s^0\right), \qquad (24)$$

with: R_s being the gas constant of species "s" and h_s^0 being the formation enthalpy of species "s" in J/kg. The species formation enthalpy per g-mol of species is specified in Tab. 1.

Table 1 Species formation enthalpy.

Species	N	O	N_2	O_2	NO
h^0 (J/g-mol)[1]	470,816.0	246,783.0	0.0	0.0	90,671.0

(1) As can be noted, dividing each above term by the species molecular mass and multiplying by 10^3, it is possible to obtain the formation enthalpy in J/kg.

(b) Mixture rotational internal energy:

$$e_R = \sum_{s=1}^{ns} e_{R,s}\sigma_s = \sum_{s=mol}\left[\int_o^T C_{v,R,s}(T')dT'\right]\sigma_s = \sum_{s=mol}\sigma_s\int_o^T C_{v,R,s}(T')dT' \quad (25)$$

where: $e_{R,s}$ is the rotational internal energy per kg-mol of species "s", in J/kg-mol. The specific heat at constant volume per kg-mol of species "s" due to rotation, in J/(kg-mol.K), is defined by:

$$C_{v,R,s} = R \Rightarrow e_{R,s}(T) = RT \therefore e_R(T) = \sum_{s=mol}\sigma_s RT$$
$$\text{or } e_R(T) = \sum_{s=mol} c_s R_s T, \quad (26)$$

with e_R being the rotational internal energy per unity of gaseous mixture mass, in J/kg.

(c) Mixture vibrational internal energy:

$$e_V = \sum_{s=mol} e_{v,s}\sigma_s = \sum_{s=mol}\sigma_s\int_o^{T_V} C_{v,V,s}(T')dT'; \text{ with}$$
$$C_{v,V,s} = C_{v,V,s}(T_v) = R\frac{e^{\theta_{V,s}/T_V}}{\left(e^{\theta_{V,s}/T_V}-1\right)^2}\left(\frac{\theta_{v,s}}{T_v}\right)^2, \quad (27)$$

in which: e_V is the vibrational internal energy per unity of gaseous mixture mass, in J/kg; $e_{v,s}$ is the vibrational internal energy per kg-mol of species "s", in J/kg-mol; $C_{v,V,s}$ is the specific heat at constant volume per kg-mol of species "s" due to vibration, in J/(kg-mol.K); $\theta_{v,s}$ is the characteristic vibrational temperature of species "s", in K; and T_v is the vibrational temperature, in K. The characteristic vibrational temperature to each molecule is specified in Tab. 2, obtained from [4]. It is important to note that e_V is also directly obtained from the vector of conserved variables.

Table 2 Characteristic vibrational temperature of the molecular species.

Species	N_2	O_2	NO
$\theta_{v,s}$ (K)	3,390.0	2,270.0	2,740.0

It is important to note that the modes of translational and rotational internal energy are assumed completely excited and, hence, the specific heats at constant volume to these modes are temperature independent. The vibrational-internal-energy mode is admitted not be completely excited, and, hence, the vibrational specific heat at constant volume is function of the vibrational temperature. The expression above to $C_{v,V,s}$ is due to [23] and is the result of the hypothesis that the molecules can be considered as harmonic oscillators. Note that when the mode of vibrational internal energy is completely excited, i.e., when $T_v >> \theta_{v,s}$, $C_{v,V,s}$ = R.

(c) Mixture internal energy:

$$e_{int} = e_T + e_R + e_V, \quad (28)$$

which is the internal energy per unity of mixture mass, in J/kg.

(d) Frozen speed of sound:

$$C_{v,TR} = \sum_{s=1}^{ns}\sigma_s C_{v,TR,s} = \sum_{s=1}^{ns}\sigma_s\begin{pmatrix} 2.5R & \text{molecules} \\ 1.5R & \text{atoms}\end{pmatrix};$$
$$\beta = R\sigma/C_{v,TR} \;\therefore\; a_f = \sqrt{(\beta+1)p/\rho}. \quad (29)$$

The frozen speed of sound, in a thermochemical non-equilibrium model, should be employed in the calculation of the convective flux of the [17] scheme. $C_{v,TR,s}$ is the specific heat at constant volume due to translation and rotation; in other words, $C_{v,TR,s}$ is the sum of $C_{v,T,s}$ with $C_{v,R,s}$.

(e) Determination of the translational/rotational temperature:

$$\frac{e}{\rho} = \sum_{s=1}^{ns} c_s C_{v,TR,s} T + \sum_{s=1}^{ns} c_s h_s^0 + e_V + \frac{1}{2}\left(u^2+v^2+w^2\right), \quad (30)$$

to the three-dimensional case. Hence, noting that T is constant at the right hand side of Eq. (30), it is possible to write:

$$T = \frac{1}{\sum_{s=1}^{ns} c_s C_{v,TR,s}} \left[\frac{e}{\rho} - \sum_{s=1}^{ns} c_s h_s^0 - e_V - \frac{1}{2}\left(u^2 + v^2 + w^2\right) \right], \quad (31)$$

to the three-dimensional case;

(f) Determination of the vibrational temperature:

The vibrational temperature is calculated through an interactive process employing the Newton-Raphson method (details in [24]).

(g) Species pressure:

Applying the equation of a thermally perfect gas to each species:

$$p_s = \rho_s R_s T, \quad (32)$$

where: $\rho_s = c_s \rho$ is the density of species "s", R_s is the gas constant to species "s" and T is the translational/rotational temperature.

2.3 Transport Model/Transport Physical Properties

2.3.1 Collision integrals to species i and j

In Table 3 are presented values of $\mathrm{Log}_{10}\left[\pi\Omega_{i,j}^{(1,1)}\right]$ and $\mathrm{Log}_{10}\left[\pi\Omega_{i,j}^{(2,2)}\right]$ to temperature values of 2,000 K and 4,000 K. The indexes i and j indicate, in the present case, the collision partners; in other words, the pair formed by one atom and one atom, one atom and one molecule, etc. These data were obtained from [1].

The data aforementioned define a linear interpolation to values of $\mathrm{Log}_{10}\left[\pi\Omega_{i,j}^{(k,k)}\right]$ as function of Ln(T), with k = 1, 2, through the linear equation:

$$\mathrm{Log}_{10}\left[\pi\Omega_{i,j}^{(k,k)}\right](T) = \mathrm{Log}_{10}\left[\pi\Omega_{i,j}^{(k,k)}\right](T = 2{,}000\mathrm{K}) + slope \times \mathrm{Ln}\left(T/2{,}000\right), \quad (33)$$

in which:

$$slope = \left\{\mathrm{Log}_{10}\left[\pi\Omega_{i,j}^{(k,k)}\right](T = 4{,}000\mathrm{K}) - \mathrm{Log}_{10}\left[\pi\Omega_{i,j}^{(k,k)}\right](T = 2{,}000\mathrm{K})\right\} / \mathrm{Ln}2. \quad (34)$$

The value of $\pi\Omega_{i,j}^{(k,k)}$ is obtained from:

$$\pi\Omega_{i,j}^{(k,k)}(T) = e^{\left\{\mathrm{Log}_{10}\left[\pi\Omega_{i,j}^{(k,k)}\right](T=2{,}000\mathrm{K}) + slope \times \mathrm{Ln}\left(T/2{,}000\right)\right\} \times \mathrm{Ln}10}, \quad (35)$$

with the value of $\Omega_{i,j}^{(k,k)}$ in m^2.

Table 3 Collision integrals to five chemical species: N, O, N_2, O_2 and NO.

Pairs		$\mathrm{Log}_{10}\left[\pi\Omega_{i,j}^{(1,1)}\right]$		$\mathrm{Log}_{10}\left[\pi\Omega_{i,j}^{(2,2)}\right]$	
I	j	2,000 K	4,000 K	2,000 K	4,000 K
N	N	-14.08	-14.11	-14.74	-14.82
N	O	-14.76	-14.86	-14.69	-14.80
N	N_2	-14.67	-14.75	-14.59	-14.66
N	O_2	-14.66	-14.74	-14.59	-14.66
N	NO	-14.66	-14.75	-14.67	-14.66
O	N	-14.76	-14.86	-14.69	-14.80
O	O	-14.11	-14.14	-14.71	-14.79
O	N_2	-14.63	-14.72	-14.55	-14.64
O	O_2	-14.69	-14.76	-14.62	-14.69
O	NO	-14.66	-14.74	-14.59	-14.66
N_2	N	-14.67	-14.75	-14.59	-14.66
N_2	O	-14.63	-14.72	-14.55	-14.64
N_2	N_2	-14.56	-14.65	-14.50	-14.58
N_2	O_2	-14.58	-14.63	-14.51	-14.54
N_2	NO	-14.57	-14.64	-14.51	-14.56
O_2	N	-14.66	-14.74	-14.59	-14.66
O_2	O	-14.69	-14.76	-14.62	-14.69
O_2	N_2	-14.58	-14.63	-14.51	-14.54
O_2	O_2	-14.60	-14.64	-14.54	-14.57
O_2	NO	-14.59	-14.63	-14.52	-14.56

Table 3 Collision integrals to five chemical species: N, O, N_2, O_2 and NO (Continuation).

Pairs		$\text{Log}_{10}\left[\pi\Omega_{i,j}^{(1,1)}\right]$		$\text{Log}_{10}\left[\pi\Omega_{i,j}^{(2,2)}\right]$	
I	j	2,000 K	4,000 K	2,000 K	4,000 K
NO	N	-14.66	-14.75	-14.67	-14.66
NO	O	-14.66	-14.74	-14.59	-14.66
NO	N_2	-14.57	-14.64	-14.51	-14.56
NO	O_2	-14.59	-14.63	-14.52	-14.56
NO	NO	-14.58	-14.64	-14.52	-14.56

2.3.2 Modified collision integrals to the species i and j

[1] and [4] define the modified collision integrals to the species i and j as:

$$\Delta_{i,j}^{(1)}(T)=\frac{8}{3}\sqrt{\frac{2m_{i,j}}{\pi RT}}\pi\Omega_{i,j}^{(1,1)} \quad \text{and} \quad \Delta_{i,j}^{(2)}(T)=\frac{16}{5}\sqrt{\frac{2m_{i,j}}{\pi RT}}\pi\Omega_{i,j}^{(2,2)}, \tag{36}$$

with:

$$m_{i,j}=M_iM_j/\left(M_i+M_j\right), \tag{37}$$

being the reduced molecular mass. These integrals are given in m.s. With the definition of the modified collision integrals to species i and j, it is possible to define the mixture transport properties (viscosity and thermal conductivities) and the species diffusion property (diffusion coefficient).

2.3.3 Mixture molecular viscosity

[4] define the mixture molecular viscosity as:

$$\mu_{mixt}=\sum_{i=1}^{ns}\frac{m_i\sigma_i}{\sum_{j=1}^{ns}\sigma_j\Delta_{i,j}^{(2)}(T)}, \tag{38}$$

where:

$$m_i=M_i/N_{AV}, \tag{39}$$

being the mass of a species particle under study; N_{AV} = 6.022045x10^{23} particles/g-mol, Avogadro number.

This mixture molecular viscosity is given in kg/(m.s).

2.3.4 Vibrational, frozen, rotational and translational thermal conductivities

All thermal conductivities are expressed in J/(m.s.K). [4] defines the mixture vibrational, rotational and translational thermal conductivities, as also the species diffusion coefficient, as follows.

(a) Translational thermal conductivity:

The mode of translational internal energy is admitted completely excited; hence, the thermal conductivity of the translational internal energy is determined by:

$$k_T=\frac{15}{4}k_{Boltzmann}\sum_{i=1}^{ns}\frac{\sigma_i}{\sum_{j=1}^{ns}\bar{a}_{i,j}\sigma_j\Delta_{i,j}^{(2)}(T)}, \tag{40}$$

in which:

$k_{Boltzmann}$ = Boltzmann constant = 1.380622x10^{-23}J/K;

$$\bar{a}_{i,j}=1+\frac{(1-M_i/M_j)\left[0.45-2.54\left(M_i/M_j\right)\right]}{\left(1+M_i/M_j\right)^2}. \tag{41}$$

(b) Rotational thermal conductivity:

The mode of rotational internal energy is also considered fully excited; hence, the thermal conductivity due to rotational internal energy is defined by:

$$k_R=k_{Boltzmann}\sum_{i=mol}^{ns}\frac{\sigma_i}{\sum_{j=1}^{ns}\sigma_j\Delta_{i,j}^{(1)}(T)}. \tag{42}$$

(c) Frozen thermal conductivity:

$$k_f=k_T+k_R. \tag{43}$$

(d) Thermal conductivity due to molecular vibration:

The mode of vibrational internal energy, however, is assumed be partially excited; hence, the vibrational thermal conductivity is calculated according to [3] by:

$$k_V = k_{Boltzmann} \sum_{i=mol} \frac{(C_{v,V,i}/R)\sigma_i}{\sum_{j=1}^{ns} \sigma_j \Delta_{i,j}^{(1)}(T)}, \quad (44)$$

with $C_{v,V,i}$ obtained from Eq. (27).

2.3.5 Species diffusion coefficient

The mass-diffusion-effective coefficient, D_i, of the species "i" in the gaseous mixture is defined by:

$$D_i = \frac{\sigma^2 M_i (1-\sigma_i M_i)}{\sum_{j=1}^{ns} \sigma_j / D_{i,j}} \quad \text{and} \quad D_{i,j} = \frac{k_{Boltzmann} T}{p \Delta_{i,j}^{(1)}(T)}, \quad (45)$$

where: $D_{i,j}$ is the binary diffusion coefficient to a pair of particles of the species "i" and "j" and is related with the modified collision integral conform described above, in Eq. (45). This coefficient is measured in m^2/s.

2.4 Chemical Model

The chemical model employed to the case of thermochemical non-equilibrium is the same employed to the case of thermal equilibrium and chemical non-equilibrium (see [21-22]). The unique difference is in the calculation of the species production rates, where a temperature of reaction rate control is introduced in the place of the translational/rotational temperature, which is employed in the calculation of such rates in the thermal equilibrium and chemical non-equilibrium case. This procedure aims a couple between vibration and dissociation. This temperature is defined as: $T_{rrc} = \sqrt{T \times T_v}$, where T is the translational/rotational temperature and T_v is the vibrational temperature. This temperature T_{rrc} replaces the translational/rotational temperature in the calculation of the species production rates, according to [25].

2.4.1 Law of Mass Action

The symbolic representation of a given reaction in the present work follows the [26] formulation and is represented by:

$$\sum_{s=1}^{ns} \upsilon'_{sr} A_s \leftrightarrow \sum_{s=1}^{ns} \upsilon''_{sr} A_s \text{ , r = 1,..., nr.} \quad (46)$$

The law of mass action applied to this system of chemical reactions is defined by:

$$\dot{\omega}_s = M_s \sum_{r=1}^{nr} (\upsilon''_{sr} - \upsilon'_{sr}) \left\{ k_{fr} \prod_{s=1}^{ns} \left(\frac{\rho_s}{M_s} \right)^{\upsilon'_{sr}} - k_{br} \prod_{s=1}^{ns} \left(\frac{\rho_s}{M_s} \right)^{\upsilon''_{sr}} \right\}, \quad (47)$$

where A_s represents the chemical symbol of species "s", "ns" is the number of species of the present study (reactants and products) involved in the considered reaction; "nr" is the number of reactions considered in the chemical model; υ'_{sr} e υ''_{sr} are the stoichiometric coefficients to reactants and products, respectively; $k_{fr} = AT^B e^{-C/T}$ and $k_{br} = DT^{-E}$, with A, B, C, D and E being constants of a specific chemical reaction under study ["fr" = forward reaction and "br" = backward reaction].

Table 4. Chemical reactions and forward coefficients.

Reaction	Forward reaction rate coefficients, k_{fr}, $cm^3/(mol.s)$	Third body
$O_2+M \leftrightarrow 2O+M$	$3.61x10^{18}T^{-1.0}e^{(-59,400/T)}$	O, N, O_2, N_2, NO
$N_2+M \leftrightarrow 2N+M$	$1.92x10^{17}T^{-0.5}e^{(-113,100/T)}$	O, O2, N_2, NO
$N_2+N \leftrightarrow 2N+N$	$4.15x10^{22}T^{-0.5}e^{(-113,100/T)}$	-
$NO+M \leftrightarrow N+O+M$	$3.97x10^{20}T^{-1.5}e^{(-75,600/T)}$	O, N, O_2, N_2, NO
$NO+O \leftrightarrow O_2+N$	$3.18x10^{9}T^{1.0}e^{(-19,700/T)}$	-
$N_2+O \leftrightarrow NO+N$	$6.75x10^{13}e^{(-37,500/T)}$	-

It is important to note that $k_{br} = k_{fr}/k_{er}$, with k_{er} being the equilibrium constant which depends only of the thermodynamic quantities. In this work, ns = 5 and nr = 17. Table 4 presents the values to A, B, C, D and E for the forward reaction rates of the 17 chemical reactions. Table 5 presents the values to A, B, C, D and E for the backward reaction rates.

Table 5. Chemical reactions and backward coefficients.

Reaction	Backward reaction rate coefficients, k_{br}, $cm^3/(mol.s)$ or $cm^6/(mol^2.s)$	Third body
$O_2+M\leftrightarrow 2O+M$	$3.01x10^{15}T^{-0.5}$	O, N, O_2, N_2, NO
$N_2+M\leftrightarrow 2N+M$	$1.09x10^{16}T^{-0.5}$	O, O2, N_2, NO
$N_2+N\leftrightarrow 2N+N$	$2.32x10^{21}T^{-0.5}$	-
$NO+M\leftrightarrow N+O+M$	$1.01x10^{20}T^{-1.5}$	O, N, O_2, N_2, NO
$NO+O\leftrightarrow O_2+N$	$9.63x10^{11}T^{0.5}e^{(-3,600/T)}$	-
$N_2+O\leftrightarrow NO+N$	$1.5x10^{13}$	-

2.5 Vibrational Model

The vibrational internal energy of a molecule, in J/kg, is defined by:

$$e_{v,s} = \frac{R_s \theta_{v,s}}{e^{\theta_{V,s}/T_V} - 1}, \qquad (48)$$

obtained by the integration of Eq. (27), and the vibrational internal energy of all molecules is given by:

$$e_V = \sum_{s=mol} c_s e_{v,s} \, . \qquad (49)$$

The heat flux due to translational-vibrational relaxation, according to [27], is given by:

$$q_{T-V,s} = \rho_s \frac{e^*_{v,s}(T) - e_{v,s}(T_v)}{\tau_s}, \qquad (50)$$

where: $e^*_{v,s}$ is the vibrational internal energy calculated at the translational temperature to the species "s"; and τ_s is the translational-vibrational relaxation time to the molecular species, in s. The relaxation time is the time of energy exchange between the translational and vibrational molecular modes.

2.5.1 Vibrational characteristic time of [28]

According to [28], the relaxation time of molar average of [29] is described by:

$$\tau_s = \tau_s^{M-W} = \sum_{l=1}^{ns} X_l \Big/ \sum_{l=1}^{ns} X_l / \tau_{s,l}^{M-W}, \qquad (51)$$

with:

$\tau_{s,l}^{M-W}$ is the relaxation time between species of [29];

τ_s^{M-W} is the vibrational characteristic time of [29];

$$X_l = c_l / (N_{AV} m_l) \quad \text{and} \quad m_l = M_l / N_{AV} \, . \qquad (52)$$

2.5.2 Definition of $\tau_{s,l}^{M-W}$:

For temperatures inferior to or equal to 8,000 K, [29] give the following semi-empirical correlation to the vibrational relaxation time due to inelastic collisions:

$$\tau_{s,l}^{M-W} = \left(\frac{B}{p_l}\right) e^{\left[A_{s,l}\left(T^{-1/3} - 0.015\mu_{s,l}^{1/4}\right) - 18.42\right]}, \qquad (53)$$

where:

$B = 1.013x10^5 Ns/m^2$ ([30]);

p_l is the partial pressure of species "l" in N/m^2;

$$A_{s,l} = 1.16x10^{-3} \mu_{s,l}^{1/2} \theta_{v,s}^{4/3} \text{ ([30]);} \qquad (54)$$

$$\mu_{s,l} = \frac{M_s M_l}{M_s + M_l}, \qquad (55)$$

being the reduced molecular mass of the collision partners: kg/kg-mol;

T and $\theta_{v,s}$ in Kelvin.

2.5.3 [25] correction time

For temperatures superiors to 8,000 K, the Eq. (53) gives relaxation times less than those observed in experiments. To temperatures above 8,000 K, [25] suggests the following relation to the vibrational relaxation time:

$$\tau_s^P = \frac{1}{\xi_s \sigma_v n_s}, \quad (56)$$

where:

$$\xi_s = \sqrt{\frac{8R_s T}{\pi}}, \quad (57)$$

being the molecular average velocity in m/s;

$$\sigma_v = 10^{-20}\left(\frac{50{,}000}{T}\right)^2, \quad (58)$$

being the effective collision cross-section to vibrational relaxation in m^2; and

$$n_s = \rho_s / m_s, \quad (59)$$

being the density of the number of collision particles of species "s". ρ_s in kg/m^3 and m_s in kg/particle, defined by Eq. (39).

Combining the two relations, the following expression to the vibrational relaxation time is obtained:

$$\tau_s = \tau_s^{M-W} + \tau_s^P. \quad (60)$$

[25] emphasizes that this expression [Eq. (60)] to the vibrational relaxation time is applicable to a range of temperatures much more vast.

3 Structured [17] Algorithm to Thermochemical Non-Equilibrium

Considering the three-dimensional and structured case, the algorithm follows that described in [22], considering, however, the vibrational contribution ([31]) and the version of the two-temperature model to the frozen speed of sound [Eq. (29)]. Hence, the discrete-dynamic-convective flux is defined by:

$$R_{i+1/2,j,k} = |S|_{i+1/2,j,k}\left\{\frac{1}{2}M_{i+1/2,j,k}\left[\begin{pmatrix}\rho a\\ \rho au\\ \rho av\\ \rho aw\\ \rho aH\end{pmatrix}_L + \begin{pmatrix}\rho a\\ \rho au\\ \rho av\\ \rho aw\\ \rho aH\end{pmatrix}_R\right]\right. - \left.\frac{1}{2}\phi_{i+1/2,j,k}\left[\begin{pmatrix}\rho a\\ \rho au\\ \rho av\\ \rho aw\\ \rho aH\end{pmatrix}_R - \begin{pmatrix}\rho a\\ \rho au\\ \rho av\\ \rho aw\\ \rho aH\end{pmatrix}_L\right]\right\} + \begin{pmatrix}0\\ S_x p\\ S_y p\\ S_z p\\ 0\end{pmatrix}_{i+1/2,j,k}, \quad (61a)$$

$$- \frac{1}{2}\phi_{i+1/2,j,k}\left[\begin{pmatrix}\rho a\\ \rho au\\ \rho av\\ \rho aw\\ \rho aH\end{pmatrix}_R - \begin{pmatrix}\rho a\\ \rho au\\ \rho av\\ \rho aw\\ \rho aH\end{pmatrix}_L\right]\right\} + \begin{pmatrix}0\\ S_x p\\ S_y p\\ S_z p\\ 0\end{pmatrix}_{i+1/2,j,k}, \quad (61b)$$

the discrete-chemical-convective flux is defined by:

$$R_{i+1/2,j,k} = |S|_{i+1/2,j,k}\left\{\frac{1}{2}M_{i+1/2,j,k}\left[\begin{pmatrix}\rho_1 a\\ \rho_2 a\\ \rho_4 a\\ \rho_5 a\end{pmatrix}_L + \begin{pmatrix}\rho_1 a\\ \rho_2 a\\ \rho_4 a\\ \rho_5 a\end{pmatrix}_R\right]\right.$$
$$\left. - \frac{1}{2}\phi_{i+1/2,j,k}\left[\begin{pmatrix}\rho_1 a\\ \rho_2 a\\ \rho_4 a\\ \rho_5 a\end{pmatrix}_R - \begin{pmatrix}\rho_1 a\\ \rho_2 a\\ \rho_4 a\\ \rho_5 a\end{pmatrix}_L\right]\right\}, \quad (62)$$

and the discrete-vibrational-convective flux is determined by:

$$R_{i+1/2,j,k} = |S|_{i+1/2,j,k}\left\{\frac{1}{2}M_{i+1/2,j,k}\left[(\rho e_v a)_L + (\rho e_v a)_R\right]\right.$$
$$\left. - \frac{1}{2}\phi_{i+1/2,j,k}\left[(\rho e_v a)_R - (\rho e_v a)_L\right]\right\}. \quad (63)$$

The same definitions presented in [21-22] are valid to this algorithm. The time integration is performed employing the Runge-Kutta explicit method of five stages, second-order accurate, to the three types of convective flux. To the dynamic part, this method can be represented in general form by:

$$\begin{aligned} Q_{i,j,k}^{(0)} &= Q_{i,j,k}^{(n)} \\ Q_{i,j,k}^{(m)} &= Q_{i,j,k}^{(0)} - \alpha_m \Delta t_{i,j,k} R\left(Q_{i,j,k}^{(m-1)}\right)/V_{i,j,k}, \\ Q_{i,j,k}^{(n+1)} &= Q_{i,j,k}^{(m)} \end{aligned} \quad (64)$$

to the chemical part, it can be represented in general form by:

$$\begin{aligned} Q_{i,j,k}^{(0)} &= Q_{i,j,k}^{(n)} \\ Q_{i,j,k}^{(m)} &= Q_{i,j,k}^{(0)} - \alpha_m \Delta t_{i,j,k}\left[R\left(Q_{i,j,k}^{(m-1)}\right)/V_{i,j,k} - S_C\left(Q_{i,j,k}^{(m-1)}\right)\right], \\ Q_{i,j,k}^{(n+1)} &= Q_{i,j,k}^{(m)} \end{aligned} \quad (65)$$

where the chemical source term S_C is calculated with the temperature T_{rrc}. Finally, to the vibrational part:

$$Q_{i,j,k}^{(0)} = Q_{i,j,k}^{(n)}$$
$$Q_{i,j,k}^{(m)} = Q_{i,j,k}^{(0)} - \alpha_m \Delta t_{i,j,k} \left[R\left(Q_{i,j,k}^{(m-1)}\right) / V_{i,j,k} - S_v\left(Q_{i,j,k}^{(m-1)}\right) \right],$$
$$Q_{i,j,k}^{(n+1)} = Q_{i,j,k}^{(m)} \qquad (66)$$

in which:

$$S_v = \sum_{s=mol} q_{T-V,s} + \sum_{s=mol} S_{C,s} e_{v,s} ; \qquad (67)$$

m = 1,...,5; $\alpha_1 = 1/4$, $\alpha_2 = 1/6$, $\alpha_3 = 3/8$, $\alpha_4 = 1/2$ and $\alpha_5 = 1$. This scheme is first-order accurate in space and second-order accurate in time. The second-order of spatial accuracy is obtained by the "MUSCL" procedure (details in [32]).

The [17] scheme in its first-order two-dimensional unstructured version to an ideal gas formulation is presented in [33]. The extension to reactive flow in thermochemical non-equilibrium in three-dimensions can be deduced from the present code.

The viscous formulation follows that of [34], which adopts the Green theorem to calculate primitive variable gradients. The viscous vectors are obtained by arithmetical average between cell (i,j,k) and its neighbours. As was done with the convective terms, there is a need to separate the viscous flux in three parts: dynamical viscous flux, chemical viscous flux and vibrational viscous flux. The dynamical part corresponds to the first five equations of the Navier-Stokes ones, the chemical part corresponds to the following four equations and the vibrational part corresponds to the last equation. The spatially variable time step technique has provided excellent convergence gains as demonstrated in [18-19] and is implemented in the code presented in this work.

4 Graphical Representation in 3D

A graphical representation of the hexahedral computational cell of volume $V_{i,j,k}$, with its respective nodes, is presented in Fig. 1.

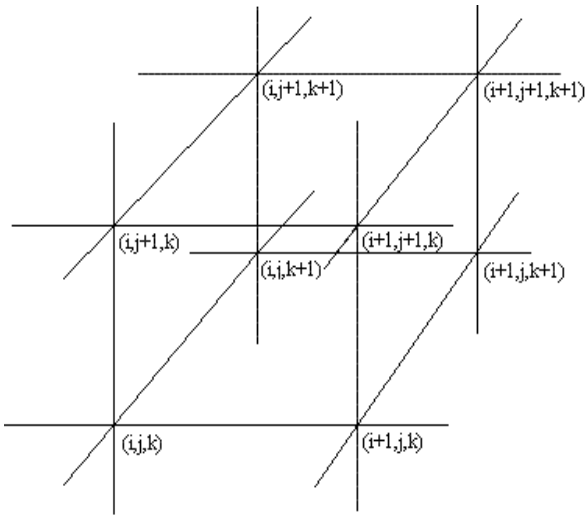

Fig. 1 Structured computational cell and respective nodes.

This computational cell is formed by the following nodes: (i,j,k), (i+1,j,k), (i+1,j+1,k), (i,j+1,k), (i,j,k+1), (i+1,j,k+1), (i+1,j+1,k+1) and (i,j+1,k+1). The calculation of the cell volume is based, in the more general case, in the determination of the volume of a deformed hexahedron in the three-dimensional space. This volume is specified by the summation of the volumes of the six (6) tetrahedrons which composes the given hexahedron. Figure 2 exhibit the division of a hexahedron in its six component tetrahedrons, as also the vertex nodes which defines each tetrahedron.

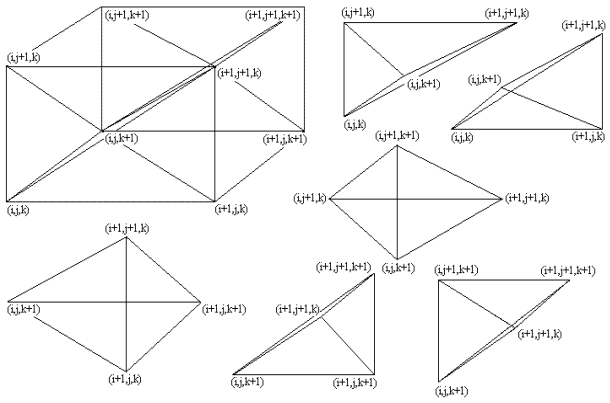

Fig. 2 Definition of a hexahedron and its six component tetrahedrons.

The volume of a tetrahedron is obtained by the calculation of the determinant below, where xP, yP, zP, xA, yA, zA, xB, yB, zB, xC, yC and zC are Cartesian coordinates of the nodes which define the tetrahedron represented in Fig. 3.

$$V_{PABC} = \frac{1}{6}\begin{vmatrix} x_P & y_P & z_P & 1 \\ x_A & y_A & z_A & 1 \\ x_B & y_B & z_B & 1 \\ x_C & y_C & z_C & 1 \end{vmatrix}, \qquad (68)$$

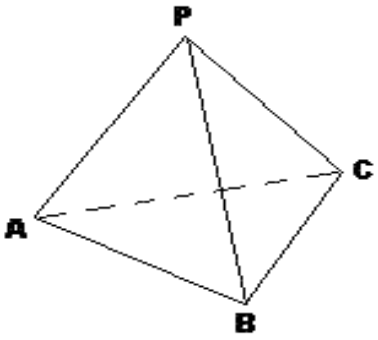

Fig. 3 Reference tetrahedron.

The hexahedron flux area is calculated by the sum of the half areas defined by the vector external product $\left|\vec{a}\,x\,\vec{b}\right|$ and $\left|\vec{c}\,x\,\vec{d}\right|$, in which $\vec{a}$, $\vec{b}$, $\vec{c}$ and $\vec{d}$ are vectors formed by the nodes which define a given flux surface, as exhibited in Fig. 4, and "×" represents the external product between vectors. The quantity $0.5\left(\left|\vec{a}\,x\,\vec{b}\right|+\left|\vec{c}\,x\,\vec{d}\right|\right)$ determines the flux area of each face, which represents nothing more than the area of a deformed rectangle.

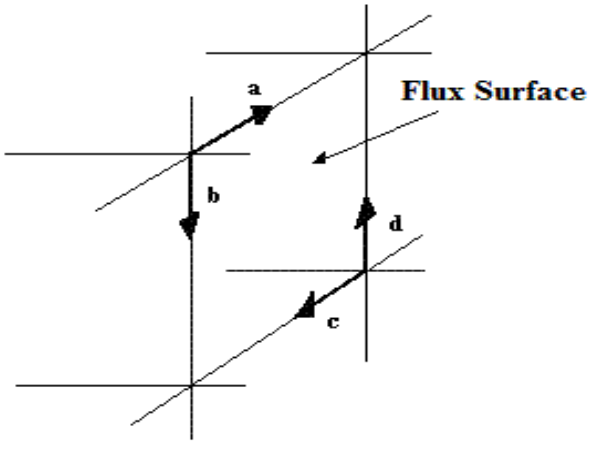

Fig. 4 Flux area (hexahedron).

The unit normal vector pointing outward to each flux face is calculated taking into account the external product of vectors $\vec{n} = \vec{a}\,x\,\vec{b} \Big/ \left|\vec{a}\,x\,\vec{b}\right|$, as exhibited in Fig. 5.

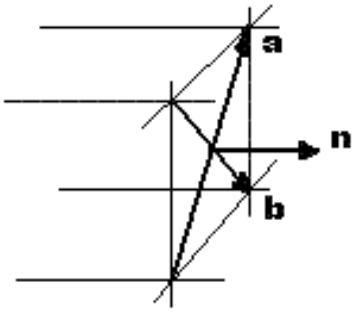

Fig. 5 Unit normal vector (hexahedron).

An additional test is necessary to verify if this vector is pointing inward or outward of the hexahedron. This test is based on the following mixed product of vectors $\left[(\vec{a}\,x\,\vec{b}) \Big/ \left|\vec{a}\,x\,\vec{b}\right|\right] \bullet \vec{f}$, where $\vec{f}$ represents the vector formed by one of the nodes of the studied flux face and one node of the hexahedron which is contained in the immediately opposed flux face, and "•" represents the vector inner product. The positive signal indicates that the normal vector is pointing inward to the hexahedron, which requires that such vector should be changed by its opposed vector.

5 MUSCL Procedure

Second order spatial accuracy can be achieved by introducing more upwind points or cells in the schemes. It has been noted that the projection stage, whereby the solution is projected in each cell face (i-1/2,j,k; i+1/2,j,k) on piecewise constant states, is the cause of the first order space accuracy of the Godunov schemes ([32]). Hence, it is sufficient to modify the first projection stage without modifying the Riemann solver, in order to generate higher spatial approximations. The state variables at the interfaces are thereby obtained from an extrapolation between neighboring cell averages. This method for the generation of second order upwind schemes based on variable extrapolation is often referred to in the literature as the MUSCL approach. The use of nonlinear limiters in such procedure, with the intention of restricting the amplitude of the gradients appearing in the solution, avoiding thus the formation of new extrema, allows that first order upwind schemes be transformed in TVD high resolution schemes with the appropriate

definition of such nonlinear limiters, assuring monotone preserving and total variation diminishing methods. Details of the present implementation of the MUSCL procedure, as well the incorporation of TVD properties to the schemes, are found in [32]. The expressions to calculate the fluxes following a MUSCL procedure and the nonlinear flux limiter definitions employed in this work, which incorporates TVD properties, are defined as follows.

The conserved variables at the interface (i+1/2,j,k) can be considered as resulting from a combination of backward and forward extrapolations. To a linear one-sided extrapolation at the interface between the averaged values at the two upstream cells (i,j,k) and (i+1,j,k), one has:

$$Q^{L}_{i+1/2,j,k} = Q_{i,j,k} + \frac{\varepsilon}{2}\left(Q_{i,j,k} - Q_{i-1,j,k}\right), \text{ (i,j,k);} \tag{69}$$

$$Q^{R}_{i+1/2,j,k} = Q_{i+1,j,k} - \frac{\varepsilon}{2}\left(Q_{i+2,j,k} - Q_{i+1,j,k}\right), \text{ (i+1,j,k),} \tag{70}$$

leading to a second order fully one-sided scheme. If the first order scheme is defined by the numerical flux

$$F_{i+1/2,j,k} = F\left(Q_{i,j,k}, Q_{i+1,j,k}\right) \tag{71}$$

the second order space accurate numerical flux is obtained from

$$F^{(2)}_{i+1/2,j,k} = F\left(Q^{L}_{i+1/2,j,k}, Q^{R}_{i+1/2,j,k}\right). \tag{72}$$

Higher order flux vector splitting methods, such as those studied in this work, are obtained from:

$$F^{(2)}_{i+1/2,j,k} = F^{+}\left(Q^{L}_{i+1/2,j,k}\right) + F^{-}\left(Q^{R}_{i+1/2,j,k}\right). \tag{73}$$

All second order upwind schemes necessarily involve at least five mesh points or cells.

To reach high order solutions without oscillations around discontinuities, nonlinear limiters are employed, replacing the term ε in Eqs. (69) and (70) by these limiters evaluated at the left and at the right states of the flux interface. To define such limiters, it is necessary to calculate the ratio of consecutive variations of the conserved variables. These ratios are defined as follows:

$$r^{+}_{i-1/2,j,k} = \left(Q_{i+1,j,k} - Q_{i,j,k}\right)/\left(Q_{i,j,k} - Q_{i-1,j,k}\right) \tag{74a}$$

$$r^{+}_{i+1/2,j,k} = \left(Q_{i+2,j,k} - Q_{i+1,j,k}\right)/\left(Q_{i+1,j,k} - Q_{i,j,k}\right), \tag{74b}$$

where the nonlinear limiters at the left and at the right states of the flux interface are defined by $\Psi^{L} = \Psi\left(r^{+}_{i-1/2,j,k}\right)$ and $\Psi^{R} = \Psi\left(1/r^{+}_{i+1/2,j,k}\right)$. In this work, five options of nonlinear limiters were considered to the numerical experiments. These limiters are defined as follows:

$$\Psi_l^{VL}(r_l) = \frac{r_l + |r_l|}{1 + r_l}, \text{ [46] limiter;} \tag{75}$$

$$\Psi_l^{VA}(r_l) = \frac{r_l + r_l^2}{1 + r_l^2}, \text{ Van Albada limiter;} \tag{76}$$

$$\Psi_l^{MIN}(r_l) = signal_l MAX\left(0, MIN\left(|r_l|, signal_l\right)\right), \text{ minmod limiter;} \tag{77}$$

$$\Psi_l^{SB}(r_l) = MAX\left(0, MIN\left(2r_l, 1\right), MIN\left(r_l, 2\right)\right), \text{ “Super Bee” limiter, due to [47];} \tag{78}$$

$$\Psi_l^{\beta-L}(r_l) = MAX\left(0, MIN\left(\beta r_l, 1\right), MIN\left(r_l, \beta\right)\right), \text{ β-limiter,} \tag{79}$$

with “l” varying from 1 to 10 (three-dimensional space), $signal_l$ being equal to 1.0 if $r_l \geq 0.0$ and -1.0 otherwise, r_l is the ratio of consecutive variations of the lth conserved variable and β is a parameter assuming values between 1.0 and 2.0, being 1.5 the value assumed in this work.

With the implementation of the numerical flux vectors following this MUSCL procedure, second order spatial accuracy and TVD properties are incorporated in the algorithms.

6 Results

Tests were performed in one personal computer “notebook” with INTEL PENTIUM DUAL CORE processor, 2.30 GHz of “clock” and 2.0 GBytes of RAM. As the interest of this work is steady state problems, it is necessary to define a criterion which guarantees the convergence of the numerical results. The criterion adopted was to consider a reduction of no minimal three (3) orders of magnitude in the value of the maximum residual in the calculation domain, a typical CFD-community criterion. The residual of each cell was defined as the numerical value obtained from the discretized conservation equations. As there are ten (10) conservation equations to each cell, the maximum value obtained from these equations is defined as the residual of this cell. Hence, this residual is compared with the residual of the other cells, calculated of the same

way, to define the maximum residual in the calculation domain. In the simulations, the attack angle was set equal to zero.

6.1 Initial and Boundary Conditions to the Studied Problem

The initial conditions are presented in Tab. 6. The Reynolds number is obtained from data of [35]. The boundary conditions to this problem of reactive flow are detailed in [24], as well the geometry in study, the meshes employed in the simulations and the description of the computational configuration.

Table 6 Initial conditions to the problem of the blunt body.

Property	Value
M_∞	8.78
ρ_∞	0.00326 kg/m^3
p_∞	687 Pa
U_∞	4,776 m/s
T_∞	694 K
$T_{v,\infty}$	694 K
altitude	40,000 m
c_N	10^{-9}
c_O	0.07955
c_{O_2}	0.13400
c_{NO}	0.05090
L	2.0 m
Re_∞	2.3885x10^6

The geometry is a blunt body with 1.0 m of nose ratio and parallel rectilinear walls. The far field is located at 20.0 times the nose ratio in relation to the configuration nose. The dimensionless employed in the Euler and Navier-Stokes equations in this study are also described in [24].

6.2 Studied Cases

Table 7 Studied cases, mesh characteristics and accuracy order.

Case	Mesh	Accuracy Order
Inviscid – 3D	63x60x10	First
Viscous – 3D	63x60x10 (7.5%)[a]	First
Inviscid – 3D	63x60x10	Second
Viscous – 3D	63x60x10 (7.5%)[a]	Second

[a] Exponential stretching..

Table 7 presents the studied cases in this work, the mesh characteristics and the order of accuracy of the [17] scheme. The unstructured results are exhibited in [40], with the presentation of the [17] scheme written to an unstructured formulation.

6.3 Results in Thermochemical Non-Equilibrium

6.3.1 Inviscid, structured and first-order accurate case

Figure 6 exhibits the pressure contours around the blunt body geometry calculated at the computational domain by the [17] scheme, in its first-order version, in thermochemical non-equilibrium. The non-dimensional pressure peak is equal to 148 unities and is located at the configuration nose. The solution presents good symmetry characteristics.

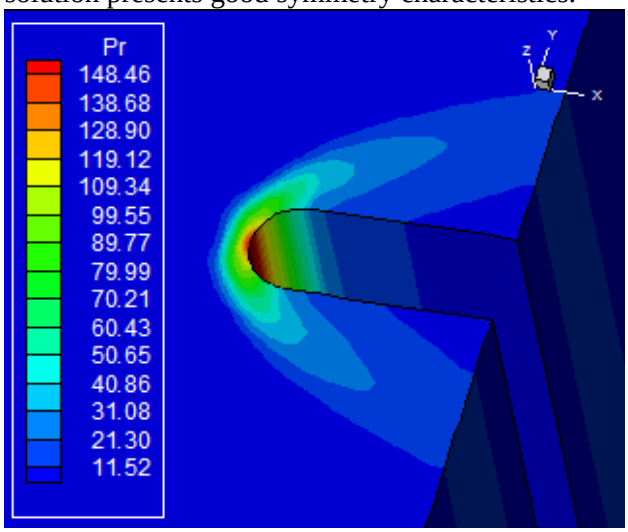

Fig. 6 Pressure contours.

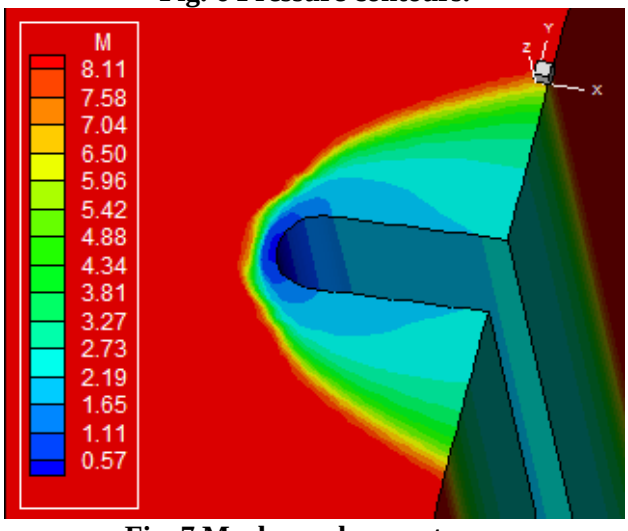

Fig. 7 Mach number contours.

Figure 7 shows the Mach number contours calculated at the computational domain. A region of subsonic flow is formed behind the normal shock wave, at the geometry nose. The shock wave develops normally: normal shock wave at the configuration nose, decaying to oblique shock

waves and finally reaching, far from the blunt body, the Mach wave.

Figure 8 presents the contours of the translational/rotational temperature distribution calculated at the computational domain. The translational/rotational temperature reaches a peak of 8,105 K at the configuration nose and determines an appropriated region to dissociation of N_2 and O_2. Along the blunt body, the translational/rotational temperature assumes an approximated value of 6,000 K, what also represents a good value to the dissociation firstly of O_2 and, in second place, of the N_2.

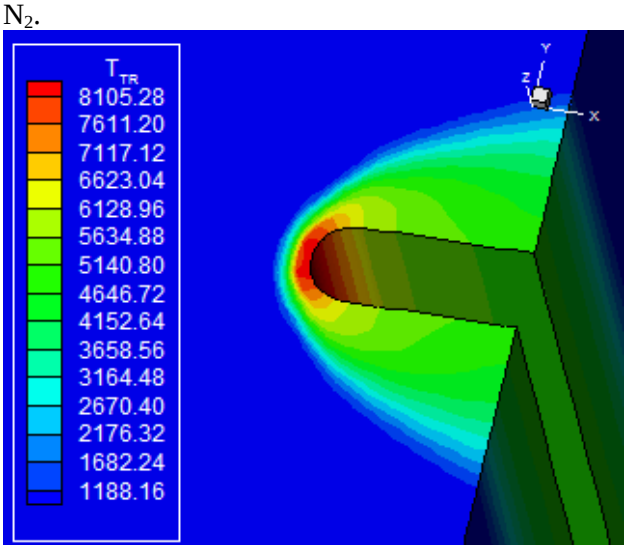

Fig. 8 T/R temperature contours.

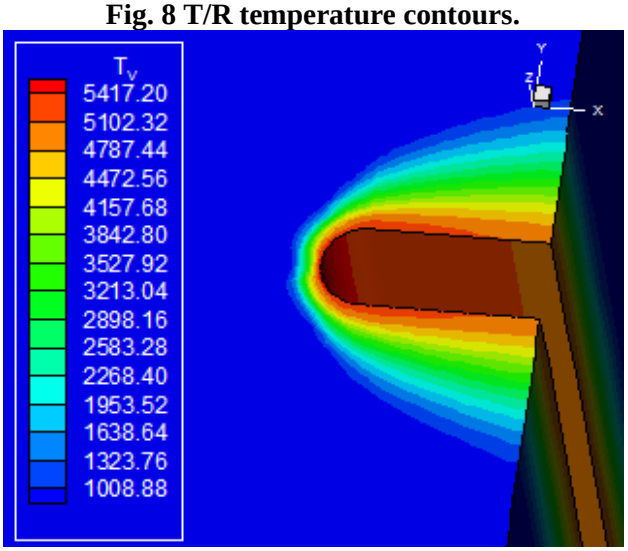

Fig. 9 Vibrational temperature contours.

Figure 9 exhibits the contours of the vibrational temperature calculated at the three-dimensional computational domain. Its peak reaches a value of 5,417 K and also contributes to the dissociation of N_2 and O_2, since the employed temperature to the calculation of the forward and backward reaction rates (reaction-rate-control temperature, T_{rrc}) in the thermochemical non-equilibrium is equal to $\sqrt{T.T_V}$, the square root of the product between the translational/rotational temperature and the vibrational temperature. Hence, the effective temperature to the calculation of the chemical phenomena guarantees the couple between the vibrational mode and the dissociation reactions. In this configuration nose region, the temperature T_{rrc} reaches, in the steady state condition, the approximated value of 6,626 K, guaranteeing that the dissociation phenomena described above occurs. Good symmetry characteristics are observed.

Figure 10 shows the mass fraction distribution of the five chemical species under study, namely: N, O, N_2, O_2 and NO, along the geometry stagnation line or geometry symmetry line. As can be observed from this figure, enough dissociation of N_2 and O_2 occur, with the consequent meaningful increase of N, of NO and of O in the gaseous mixture. As mentioned early, this behaviour is expected due to the effective peak temperature reached at the calculation domain. The NO presented the biggest absolute increase in its formation, whereas the N presented the biggest relative increase.

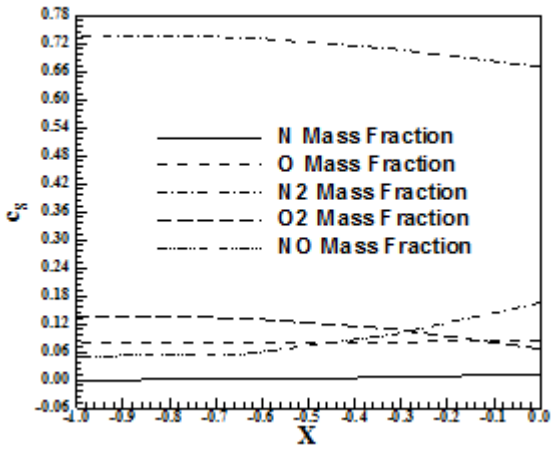

Fig. 10 Mass fraction distribution at the blunt body stagnation line.

6.3.2 Viscous, structured and first-order accurate case

Figure 11 exhibits the pressure contours to the viscous reactive flow around a blunt body, in three-dimensions, calculated at the computational domain. The non-dimensional pressure peak reaches 170 unities, more severe than that obtained with the inviscid case. The pressure field is also more severe in the viscous case than in the inviscid one. The shock is closer to the geometry due to the mesh exponential stretching and the viscous reactive effects of the simulation. The region of the pressure

peak is also better defined. The solution presents good symmetry characteristics.

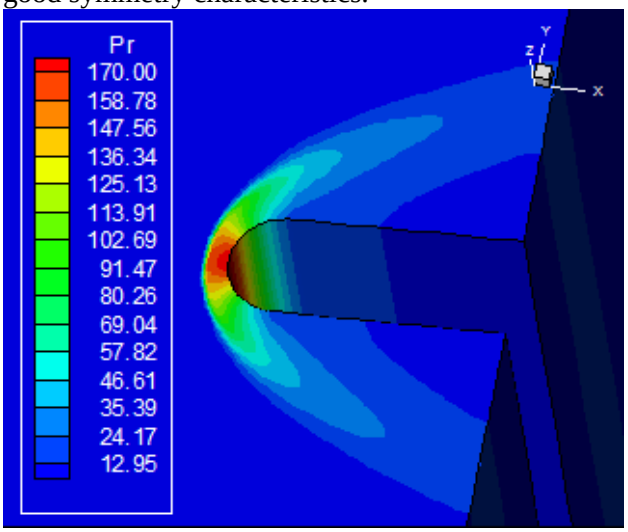

Fig. 11 Pressure contours.

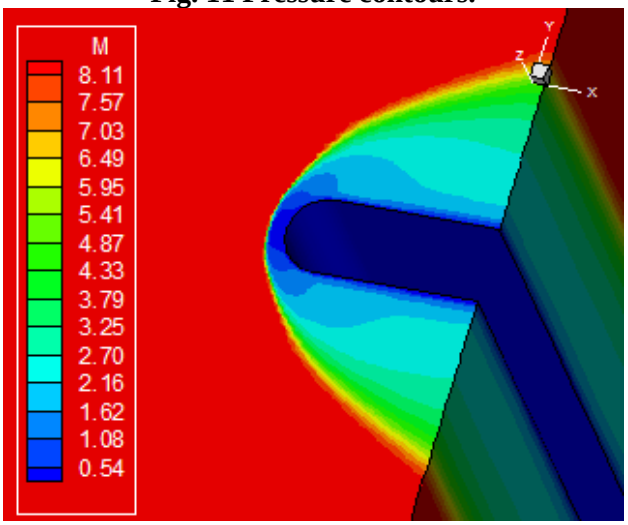

Fig. 12 Mach number contours.

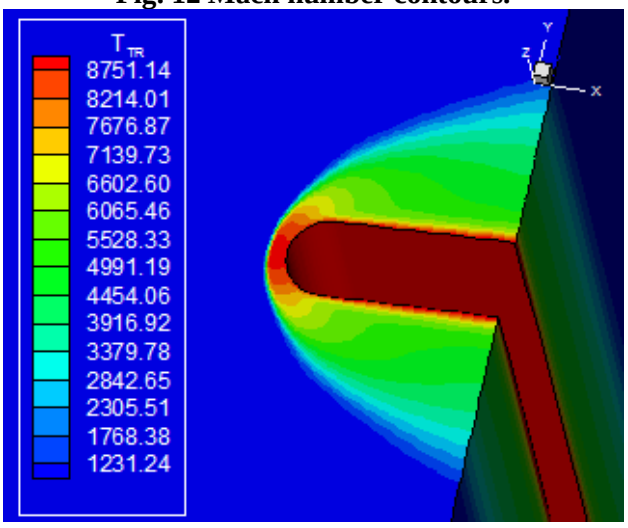

Fig. 13 T/R temperature contours.

Figure 12 shows the Mach number contours calculated at the computational domain. The subsonic flow region, which is formed behind the normal shock, is well captured and propagates by the lower and upper geometry walls, due to the transport phenomena considered in the viscous simulations. The shock wave presents the expected behaviour: normal shock wave at the configuration nose, oblique shock waves and a Mach wave far from de blunt body.

Figure 13 exhibits the distribution of the translational/rotational temperature calculated at the computational domain. The peak of translational/rotational temperature reaches the approximated value of 8,750 K at the configuration nose and this value is observed along the lower and upper surfaces of the geometry.

Figure 14 presents the vibrational temperature distribution calculated at the computational domain. Its peak, at the configuration nose, reaches an approximated value of 5,403 K. The effective temperature to the calculation of the dissociation and recombination reactions, T_{rrc}, is equal approximately to 6,876 K, which guarantees that processes of dissociation of O_2 and N_2 can be captured by the employed formulation. This value of effective temperature to the viscous reactive simulations is superior to that obtained in the inviscid case. Good symmetry characteristics are observed in these figures.

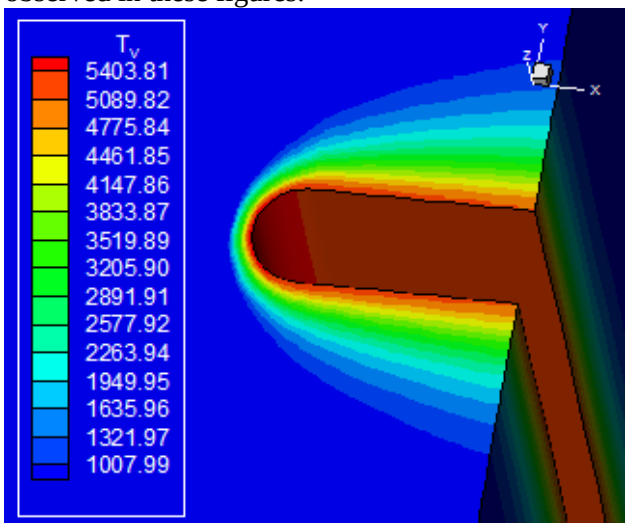

Fig. 14 Vibrational temperature contours.

Figure 15 exhibits the mass fraction distribution of the five chemical species under study along the geometry stagnation line. As can be observed, enough dissociation of the N_2 and O_2 occurs, with the consequent meaningful increase of the N, of the NO and of the O in the gaseous mixture. This behaviour is expected due to the temperature peak reached in the calculation domain. The biggest absolute increase in the formation of a species was due to the NO, while, in relative terms, was due to the N. As can also be noted, the mass fraction of the

NO tends to assume a constant value at the configuration nose. This is due to the same behaviour observed in the mass fraction distributions of the N and O, close to the configuration nose (constancy).

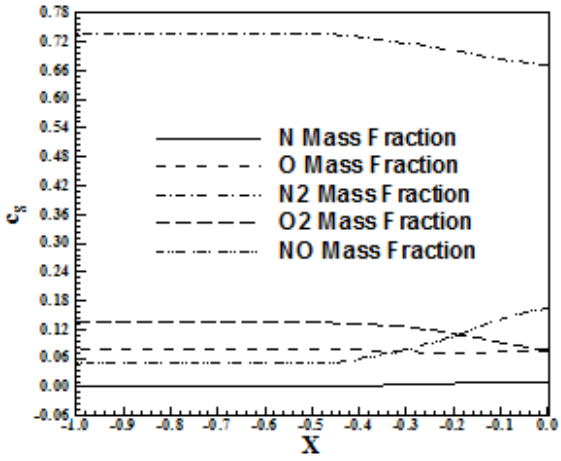

Fig. 15 Mass fraction distribution at the blunt body stagnation line.

6.3.3 Inviscid, structured and second-order accurate case

Figure 16 shows the pressure contours obtained by the inviscid simulation performed by the second-order [17] scheme employing a minmod non-linear flux limiter. The non-dimensional pressure peak is approximately equal to 145 unities, slightly inferior to the respective peak obtained by the first-order solution. This pressure peak occurs at the configuration nose. The solution presents good symmetry characteristics.

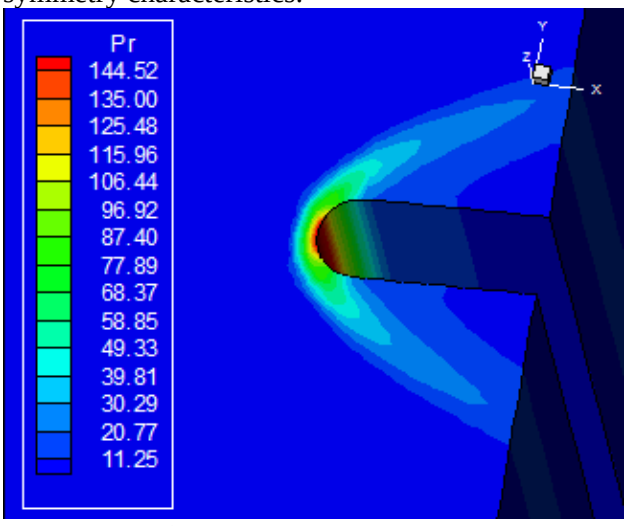

Fig. 16 Pressure contours.

Figure 17 presents the Mach number contours obtained at the computational domain. The subsonic region which is formed behind the normal shock wave is well characterized at the configuration nose. Good symmetry characteristics are observed. The shock wave presents the expected behaviour, passing from a normal shock at the configuration stagnation line to a Mach wave far from the blunt body.

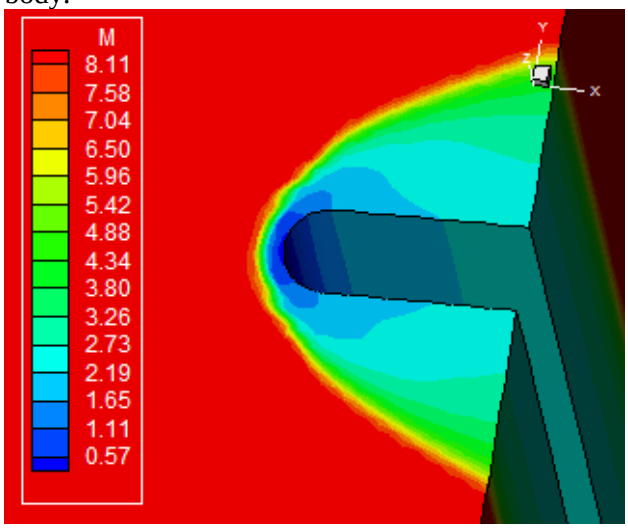

Fig. 17 Mach number contours.

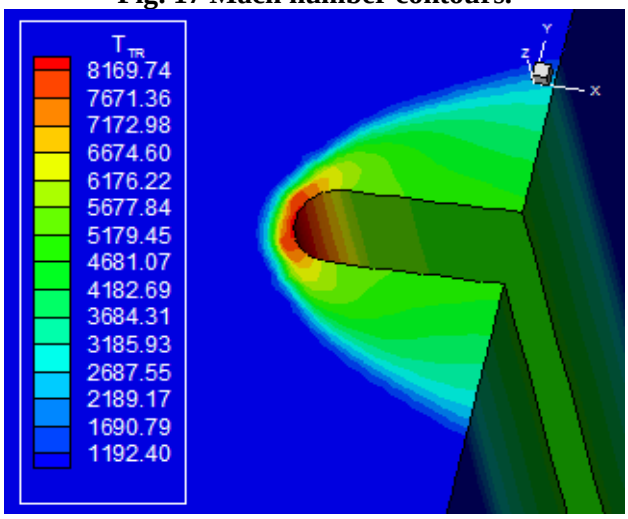

Fig. 18 T/R temperature contours.

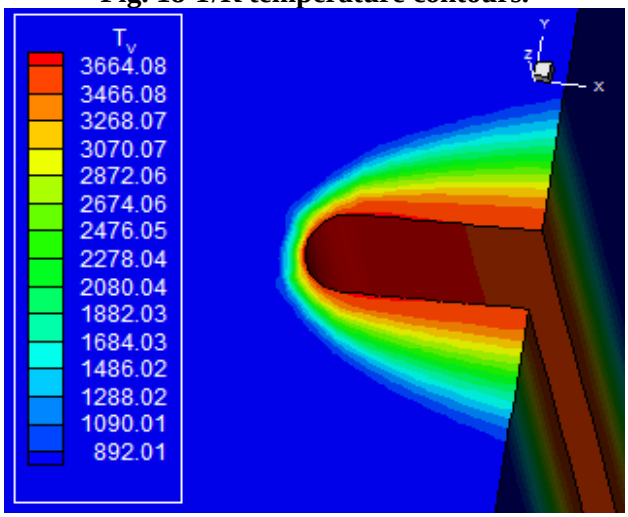

Fig. 19 Vibrational temperature contours.

Figure 18 exhibits the contours of the translational/rotational temperature distribution calculated at the computational domain. The translational/rotational temperature peak occurs at the configuration nose and is approximately equal to 8,170 K. Figure 19 presents the contours of the vibrational temperature distribution calculated at the computational domain. The vibrational temperature peak is approximately equal to 3,664 K and is observed at the configuration nose. The effective temperature to calculation of the reaction rates (reaction rate control temperature, T_{rrc}) is approximately equal to 5,471 K, which represents a temperature capable to capture the dissociation phenomena of N_2 and O_2. Good symmetry characteristics are observed in both figures.

Figure 20 exhibits the mass fraction distribution of the five chemical species under study, namely: N, O, N_2, O_2 and NO, along the geometry stagnation line. As can be observed, discrete dissociation of N_2 and O_2 occur, with consequent discrete increase of the N, of the NO and of the O in the gaseous mixture. This behaviour is expected due to the effective temperature peak reached at the computational domain to the calculation of thermochemical non-equilibrium and to a second-order numerical formulation, which behaves in a more conservative way (see [22]), providing minor dissociation of N_2 and O_2.

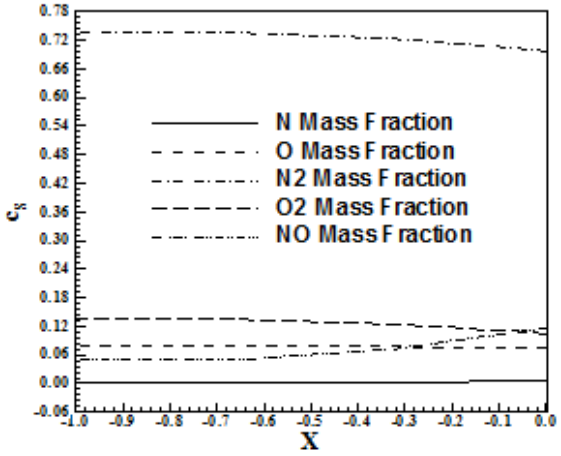

Fig. 20 Mass fraction distribution at the blunt body stagnation line.

6.3.4 Viscous, structured and second-order accurate case

Figure 21 exhibits the pressure contours calculated at the computational domain to the studied configuration of blunt body. The non-dimensional pressure peak is approximately equal to 164 unities, less than the respective value obtained by the first-order solution. The shock is positioned closer to the blunt body due to the mesh stretching and the employed-viscous-reactive formulation. Good symmetry characteristics are observed.

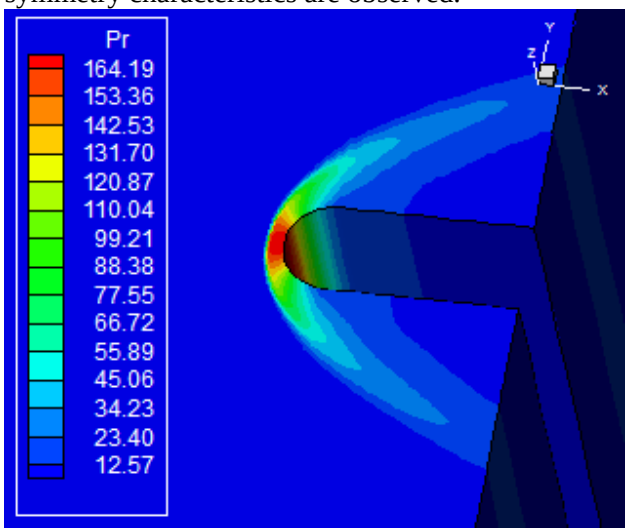

Fig. 21 Pressure contours.

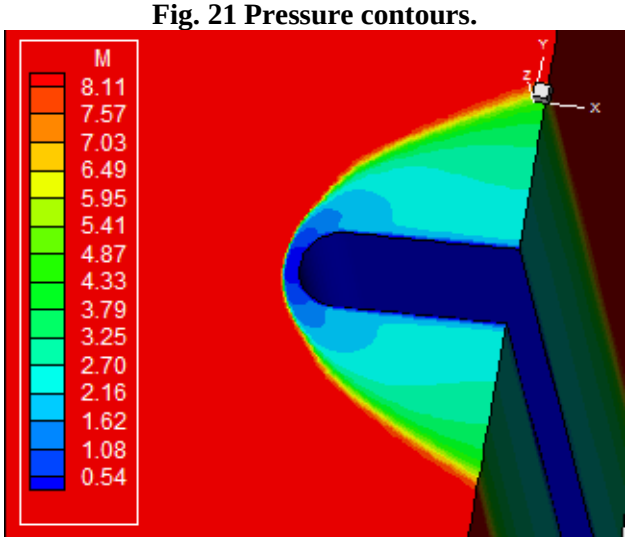

Fig. 22 Mach number contour.

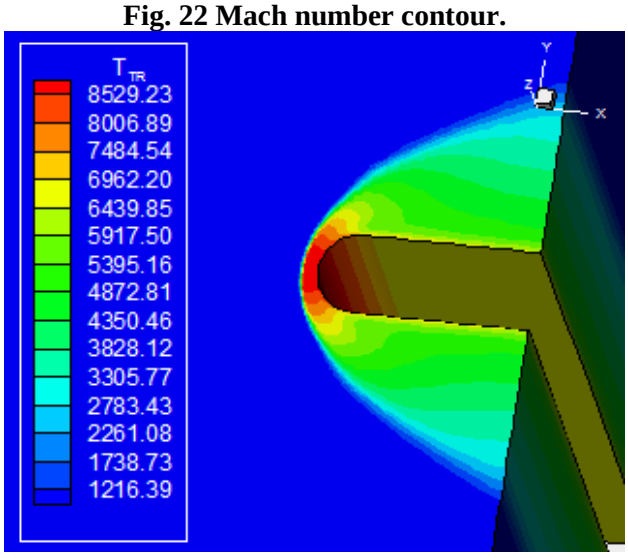

Fig. 23 T/R temperature contours.

Figure 22 shows the Mach number contours obtained at the computational domain. The subsonic

region behind the normal shock wave, at the stagnation line, is well captured by the solution. This region propagates along the lower and upper surfaces of the geometry, due to the transport phenomena (viscosity, thermal conductivity and species diffusion). The shock wave behaviour is also the expected: normal shock at the geometry nose, oblique shock waves close to the configuration and Mach wave far from the geometry.

Figure 23 exhibits the translational/rotational temperature distribution calculated at the computational domain. The temperature peak at the configuration nose reaches approximately 8,529 K. Figure 24 shows the vibrational temperature distribution calculated at the computational domain. The temperature peak at the nose and along the lower and upper surfaces of the geometry is equal to 4,230 K. The effective temperature to the calculation of the reaction rates, T_{rrc}, was of 6,006 K, superior to that obtained with the first-order solution, which is representative to the calculation of the N_2 and O_2 dissociations. Both Figs. 23 and 24 exhibit good symmetry characteristics.

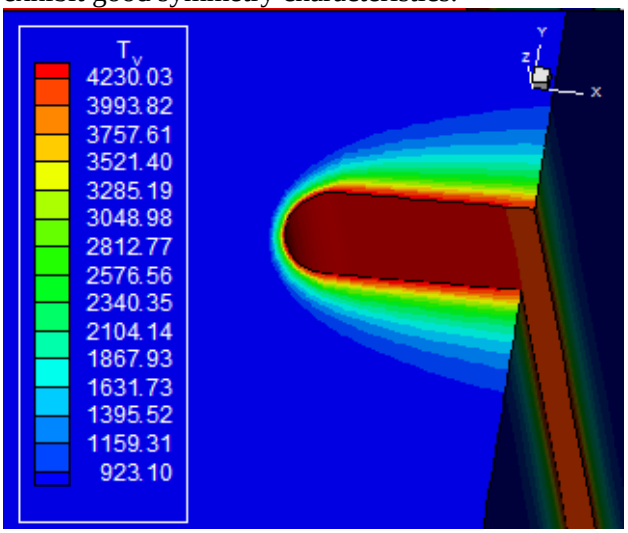

Fig. 24 Vibrational temperature contours.

Figure 25 presents the mass fraction distribution of the five chemical species under study, namely: N, O, N_2, O_2 and NO, along the geometry stagnation line. As can be observed, good dissociation of N_2 and O_2 occur, with consequent good increase of N, O and NO in the gaseous mixture. This behaviour is expected due to the effective temperature peak reached at the computational domain to the calculation of thermochemical non-equilibrium and to a second-order numerical formulation, which behaves in a more conservative way ([22]), providing major dissociation of N_2 and O_2. In other words, this solution provided by the second-order [17] scheme, as seen in other cases, tends to provide bigger dissociation of N_2 and O_2. As this solution is more precise (second-order), it should be considered as standard to comparison with other schemes.

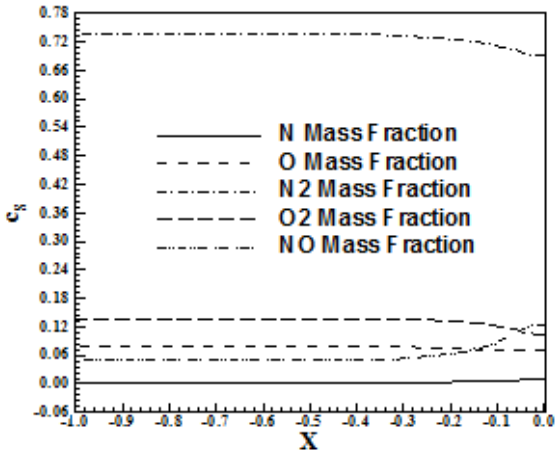

Fig. 25 Mass fraction distribution at the blunt body stagnation line.

6.4 Comparison Between Thermal Equilibrium and Chemical Non-Equilibrium Results and Thermochemical Non-Equilibrium Results

6.4.1 Shock Position

In this section is presented the behaviour of the shock position in thermal equilibrium and chemical non-equilibrium, and in thermochemical non-equilibrium conditions. First and second order results are presented.

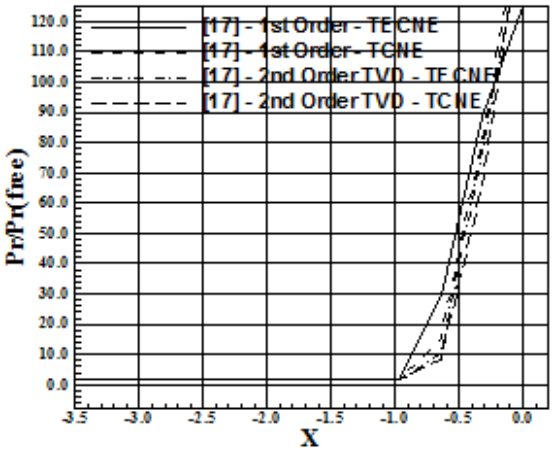

Fig. 26 Shock position (inviscid).

The detached shock position in terms of pressure distribution, in the inviscid case, is exhibited in Fig. 26. It is shown the thermal equilibrium and chemical non-equilibrium shock position ([41]), and the thermochemical non-equilibrium shock position. As can be observed, both thermal equilibrium and chemical non-equilibrium and the thermochemical

non-equilibrium cases define positions at 1.00 m, in both first and second order cases.

The detached shock position in terms of pressure distribution, in the viscous case, is exhibited in Fig. 27. It is shown the thermal equilibrium and chemical non-equilibrium shock position ([41]), and the thermochemical non-equilibrium shock position. As can be observed, the shock position detected by the thermal equilibrium and chemical non-equilibrium case is positioned at 0.55 m from the body nose; the same position detected by the thermochemical non-equilibrium case as the first order scheme is used. However, as the second order scheme is used, both thermal equilibrium and chemical non-equilibrium and thermochemical non-equilibrium cases capture the same position to the shock detachment, 0.50 m. It ratifies the best behaviour expected to the [17] scheme when its second order version is employed.

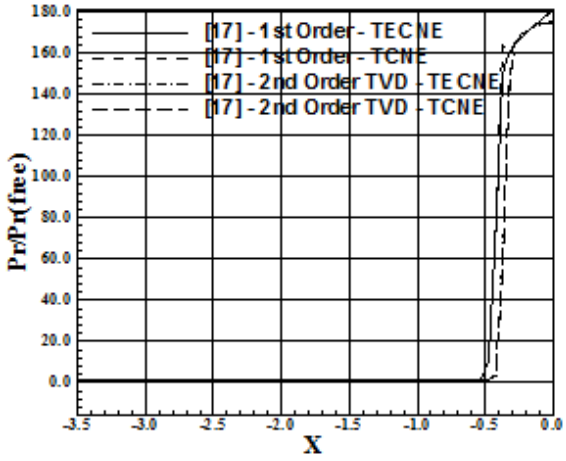

Fig. 32 Shock position (viscous).

6.4.2 Quantitative Analysis

In terms of quantitative results, the present authors compared the reactive results of thermal equilibrium and chemical non-equilibrium and the thermochemical non-equilibrium solutions. The stagnation pressure at the blunt body nose and the shock standoff distance were evaluated assuming the perfect gas formulation. Such parameters calculated at this way are not the best comparisons, but in the absence of practical reactive results, these constitute the best available results.

To calculate the stagnation pressure ahead of the blunt body, [36] presents in its B Appendix values of the normal shock wave properties ahead of the configuration. The ratio pr_0/pr_∞ is estimated as function of the normal Mach number and the stagnation pressure pr_0 can be determined from this parameter. Hence, to a freestream Mach number of 9.0 (close to 8.78), the ratio pr_0/pr_∞ assumes the value 104.8. The value of pr_∞ is determined by the following expression:

$$pr_\infty = \frac{pr_{initial}}{\rho_{initial} \times a_{initial}^2} \qquad (80)$$

In the present study, $pr_{initial}$ = 687 N/m^2, $\rho_{initial}$ = 0.004kg/m^3 and $a_{initial}$ = 317.024m/s. Considering these values, one concludes that pr_∞ = 1.709 (non-dimensional). Using the ratio obtained from [36], the stagnation pressure ahead of the configuration nose is estimated as 179.10 unities. Table 8 compares the values obtained from the simulations with this theoretical parameter and presents the numerical percentage errors. As can be observed, all solutions present percentage errors less than 20.0%, which is a reasonable estimation of the stagnation pressure. The best estimation was due to the [17] scheme, first order, structured and viscous.

Table 8 Comparisons between theoretical and numerical results.

Case	pr_0	Error (%)
Inviscid/Structured/1st Order	148.46	17.11
Viscous/Structured/1st Order	170.00	5.08
Inviscid/Structured/2nd Order	144.52	19.31
Viscous/Structured/2nd Order	164.19	8.32

Another possibility to quantify the results is the determination of the shock standoff distance. [37] presents a graphic in which is plotted the shock standoff distance of a pre-determined configuration versus the Mach number. Considering the blunt body nose approximately as a cylinder and using the value 8.78 to the Mach number, it is possible to obtain the value 0.19 to the ratio δ/d, where δ is the position of the normal shock wave in relation to the body nose and d is a characteristic length of the configuration. In the present study, d = 2.0m (diameter of the body nose) and δ = 0.38m. Table 9 presents the values obtained by δ for the different cases and the percentage errors. This table shows that the best result is obtained with the structured, viscous, second order version of [17]. As the shock standoff distance presented in [37] is more realistic, presenting smaller dependence of the perfect gas hypothesis, improved results were expected to

obtain in this study. Hence, the best solution is obtained by the [17] scheme in its second order viscous version, with an error of 5.26%.

Table 9 Shock standoff distance obtained from numerical schemes.

Case	δ_{NUM} (m)	Error (%)
Inviscid/Structured/1st Order	0.74	94.74
Viscous/Structured/1st Order	0.44	15.79
Inviscid/Structured/2nd Order	0.60	57.89
Viscous/Structured/2nd Order	0.40	5.26

6.4.3 Computational performance of the studied algorithms

Table 10 Computational data of the reactive simulations with the 3D blunt body.

Studied case	CFL	Iterations	Orders of Reduction of the Residual
First-Order/Structured/ Inviscid/TECNE(1)	0.5	291	4
First-Order/Structured/ Viscous/TECNE	0.5	1,445	4
Second-Order/Structured/ Inviscid/TECNE	0.1	6,100	3
Second-Order/Structured/ Viscous/TECNE	0.1	6,703	4
First-Order/Structured/ Inviscid/TCNE(2)	0.9	373	4
First-Order/Structured/ Viscous/TCNE	0.7	1,005	4
Second-Order/Structured/ Inviscid/TCNE	0.3	982	4
Second-Order/Structured/ Viscous/TCNE	0.3	2,412	4

(1) TECNE: Thermal Equilibrium and Chemical Non-Equilibrium; (2) TCNE: Thermal and Chemical Non-Equilibrium.

Table 10 presents the computational data of the reactive simulations performed with the [17] scheme to the problem of the blunt body in three-dimensions. The reactive simulations involved the thermal equilibrium and chemical non-equilibrium solutions obtained from [41] and the present thermochemical non-equilibrium results. In this table are exhibited the studied case, the maximum number of CFL employed in the simulation, the number of iterations to convergence and the number of orders of reduction in the magnitude of the maximum residual in relation to its initial value to convergence.

As can be observed, all test-cases converged with no minimal three (3) orders of reduction in the value of the maximum residual. The maximum numbers of CFL presented the following distribution: 0.9 in one case (12.50%), 0.7 in one case (12.50%), 0.5 in two cases (25.00%), 0.3 in two cases (25.00%) and 0.1 in two cases (25.00%). The convergence iterations did not overtake 7,000, in all studied cases. However, the time wasted in the simulations was much raised, taking until days to convergence (to four orders of reduction in the maximum residual). It is important to emphasize that all three-dimensional viscous simulations were considered laminar, without the introduction of a turbulence model, although high Reynolds number were employed in the simulations.

7 Conclusions

This work, the first part of this study, presents a numerical tool implemented to simulate inviscid and viscous flows employing the reactive gas formulation of thermochemical non-equilibrium flow in three-dimensions. The Euler and Navier-Stokes equations, employing a finite volume formulation, on the context of structured and unstructured spatial discretizations, are solved. These variants allow an effective comparison between the two types of spatial discretization aiming verify their potentialities: solution quality, convergence speed, computational cost, etc. The aerospace problem involving the "hot gas" hypersonic flow around a blunt body, in three-dimensions, is simulated.

To the simulations with unstructured spatial discretization, a structured mesh generator developed by the first author ([38]), that creates meshes of hexahedrons (3D), was employed. After that, as a pre-processing stage ([39]), such meshes were transformed in meshes of tetrahedrons. Such procedure aimed to avoid the time which would be waste with the implementation of an unstructured

generator, which was not the objective of the present work, and to obtain a generalized algorithm to the solution of the reactive equations.

In this work, first part of this study, the structured formulation of the three-dimensional Euler and Navier-Stokes reactive equations is presented. In [40], the second part of this study, it will be presented the unstructured version of the calculation algorithm in three-dimensions to complete the formulation in structured and in unstructured contexts. Unstructured solutions are presented in such paper.

The reactive simulations involved an air chemical model of five species: N, O, N_2, O_2 and NO. Seventeen chemical reactions, involving dissociation and recombination, were simulated by the proposed model. The Arrhenius formula was employed to determine the reaction rates and the law of mass action was used to determine the source terms of each gas species equation.

The results have demonstrated that the most correct value of the stagnation pressure is obtained by the [17] scheme, in its first order and viscous structured case, with an error of 5.08%. Moreover, the best value to the shock stand-off distance is estimated by the [17] scheme, second order and viscous structured case, with an error of 5.26%. In qualitative terms, the second order versions of the thermal equilibrium and chemical non-equilibrium as well the thermochemical non-equilibrium algorithms predict closest shock waves to the blunt nose than their first order counterpart.

This work, as also [40], is the continuation of the study started at [22], based on the work of [42]. Other references on the non-equilibrium reactive flows area are: [43], [44] and [45].

8 Acknowledgments

The first author acknowledges the CNPq by the financial support conceded under the form of a DTI (Industrial Technological Development) scholarship no. 384681/2011-5. He also acknowledges the infra-structure of the ITA that allowed the realization of this work.

References:

[1] P. A. Gnoffo, R. N. Gupta, and J. L. Shinn, Conservation Equations and Physical Models for Hypersonic Flows in Thermal and Chemical Nonequilibrium, *NASA TP 2867*, 1989.

[2] M. Liu and M. Vinokur, Upwind Algorithms for General Thermo-Chemical Nonequilibrium Flows, *AIAA Paper 89-0201*, 1989.

[3] R. N. Gupta, J. M. Yos, R. A. Thompson, and K. –P. Lee, A Review of Reaction Rates and Thermodynamic and Transport Properties for an 11-Species Air Model for Chemical and Thermal Nonequilibrium Calculations to 30000 K, *NASA RP-1232*, 1990.

[4] R. K. Prabhu, An Implementation of a Chemical and Thermal Nonequilibrium Flow Solver on Unstructured Meshes and Application to Blunt Bodies, *NASA CR-194967*, 1994.

[5] C. Park, Radiation Enhancement by Nonequilibrium in Earth's Atmosphere, *Journal of Spacecraft and Rockets*, Vol. 22, No. 1, 1985, pp. 27-36.

[6] C. Park, Problem of Rate Chemistry in the Flight Regimes of Aeroassissted Orbital Transfer Vehicles, *Thermal Design of Aeroassissted Orbital Transfer Vehicles*, Progress in Astronautics and Aeronautics, edited by H. F. Nelson, AIAA, NY, Vol. 96, 1985, pp. 511-537.

[7] P. A. Gnoffo, Three-Dimensional AOTV Flowfields in Chemical Nonequilibrium, *AIAA Paper 86-0230*, 1986.

[8] C. P. Li, Implicit Methods for Computing Chemically Reacting Flow, *NASA TM-58274*, 1986.

[9] J. H. Lee, Basic Governing Equations for the Flight Regimes of Aeroassisted Orbital Transfer Vehicles, *Thermal Design of Aeroassisted Transfer Vehicles*, Progress in Astronautics and Aeronautics, AIAA, Vol. 96, 1985, pp. 3-53.

[10] C. Park, Convergence of Computation of Chemically Reacting Flows, *Thermophysical Aspects of Re-entry Flows*, Progress in Astronautics and Aeronautics, edited by J. N. Moss and C. D. Scott, AIAA, NY, Vol. 103, pp. 478-513.

[11] C. Park, Assessment of Two-Temperature Kinetic Model for Dissociating and Weakly-Ionizing Nitrogen, *AIAA Paper 86-1347*, 1986.

[12] C. Park, Calculation of Nonequilibrium Radiation in the Flight Regimes of Aeroassissted Orbital Transfer Vehicles, *Thermal Design of Aeroassissted Orbital Transfer Vehicles*, Progress in Astronautics and Aeronautics, edited by H. F. Nelson, AIAA, NY, Vol. 96, 1985, pp. 395-418.

[13] C. Park, Nonequilibrium Air Radiation (NEQAIR) Program: User's Manual, *NASA TM-86707*, 1985.
[14] R. A. Allen, J. C. Camm, and J. C. Keck, Radiation from Hot Nitrogen, Research Report 102, AVCO-Everett Research Laboratory, Everett, MA, 1961.
[15] R. A. Allen, J. C. Keck, and J. C. Camm, Nonequilibrium Radiation from Shock Heated Nitrogen and a Determination of the Recombination Rate, Research Report 110, AVCO-Everett Research Laboratory, Everett, MA, 1961.
[16] R. A. Allen, Nonequilibrium Shock Front Rotational, Vibrational, and Electronic Temperature Measurements, Research Report 186, AVCO-Everett Research Laboratory, Everett, MA, 1964.
[17] B. Van Leer, Flux-Vector Splitting for the Euler Equations, *Lecture Notes in Physics*, Springer Verlag, Berlin, Vol. 170, pp. 507-512, 1982.
[18] E. S. G. Maciel, Analysis of Convergence Acceleration Techniques Used in Unstructured Algorithms in the Solution of Aeronautical Problems – Part I, *Proceedings of the XVIII International Congress of Mechanical Engineering (XVIII COBEM)*, Ouro Preto, MG, Brazil, 2005.
[19] E. S. G. Maciel, Analysis of Convergence Acceleration Techniques Used in Unstructured Algorithms in the Solution of Aerospace Problems – Part II, *Proceedings of the XII Brazilian Congress of Thermal Engineering and Sciences (XII ENCIT)*. Belo Horizonte, MG, Brazil, 2008.
[20] S. K. Saxena and M. T. Nair, An Improved Roe Scheme for Real Gas Flow, *AIAA Paper 2005-587*, 2005.
[21] E. S. G. Maciel, Relatório ao CNPq (Conselho Nacional de Desenvolvimento Científico e Tecnológico) sobre as atividades de pesquisa realizadas no período de 01/07/2008 até 30/06/2009 com relação ao projeto PDJ número 150143/2008-7, *Report to the National Council of Scientific and Technological Development (CNPq)*, São José dos Campos, SP, Brasil, 102p, 2009. [available in the website www.edissonsavio.eng.br]
[22] E. S. G. Maciel, and A. P. Pimenta, Reentry Flows in Chemical Non-Equilibrium in Two-Dimensions, *Proceedings of the 10th International Symposium on Combustion and Energy Utilization (ICCEU 2010)*, Mugla, Turkey, 2010.
[23] W. G. Vincent and C. H. Kruger Jr., *Introduction to Physical Gas Dynamics*, John Wiley & Sons, Ltd, New York, 1965.
[24] E. S. G., Maciel, Relatório ao CNPq (Conselho Nacional de Desenvolvimento Científico e Tecnológico) sobre as atividades de pesquisa realizadas no período de 01/07/2009 até 31/12/2009 com relação ao projeto PDJ número 150143/2008-7, *Report to the National Council of Scientific and Technological Development (CNPq)*, São José dos Campos, SP, Brasil, 102p, 2009. [available in the website www.edissonsavio.eng.br]
[25] C. Park, Assessment of Two-Temperature Kinetic Model for Ionizing Air, *Journal of Thermophysics and Heat Transfer*, Vol. 3, No. 13, pp. 233-244, 1989.
[26] G. Degrez, and E. Van Der Weide, Upwind Residual Distribution Schemes for Chemical Non-Equilibrium Flows, *AIAA Paper 99-3366*, 1999.
[27] L. Landau, and E. Teller, Theory of Sound Dispersion, *Physikalische Zeitschrift Der Sowjetunion*, Vol. 10, 1936, pp. 34-43.
[28] R. Monti, D. Paterna, R. Savino, and A. Esposito, Experimental and Numerical Investigation on Martian Atmosphere Entry, *AIAA Paper 2001-0751*, 2001.
[29] R. C. Millikan and D. R. White, Systematics of Vibrational Relaxation, *The Journal of Chemical Physics*, Vol. 39, No. 12, 1963, pp. 3209-3213.
[30] A. F. P. Houwing, S. Nonaka, H. Mizuno, and K. Takayama, Effects of Vibrational Relaxation on Bow Shock Stand-off Distance for Nonequilibrium Flows, *AIAA Journal*, Vol. 38, No. 9, 2000, pp. 1760-1763.
[31] D. Ait-Ali-Yahia, and W. G. Habashi, Finite Element Adaptive Method for Hypersonic Thermochemical Nonequilibrium Flows, *AIAA Journal* Vol. 35, No. 8, 1997, 1294-1302.
[32] C. Hirsch, *Numerical Computation of Internal and External Flows – Computational Methods for Inviscid and Viscous Flows*, John Wiley & Sons Ltd, 691p, 1990.
[33] E. S. G. Maciel, Comparison Between the First Order Upwind Unstructured Algorithms of Steger and Warming and of Van Leer in the Solution of the Euler Equations in Two-Dimensions, *Proceedings of the XIX International Congress of Mechanical Engineering (XIX COBEM)*, Brasília, DF, Brazil, 2007.
[34] L. N. Long, M. M. S. Khan, and H. T. Sharp, Massively Parallel Three-Dimensional Euler /

Navier-Stokes Method, *AIAA Journal*, Vol. 29, No. 5, 1991, pp. 657-666.

[35] R. W. Fox, and A. T. McDonald, *Introdução à Mecânica dos Fluidos*, Guanabara Editor, 1988.

[36] J. D. Anderson Jr., Fundamentals of Aerodynamics, McGraw-Hill, Inc., 2nd Edition, 772p, 1991.

[37] H. W. Liepmann, and A. Roshko, Elements of Gasdynamics, John Wiley & Sons, Inc., 1st Edition, 439p, 1957.

[38] E. S. G. Maciel, Relatório ao Conselho Nacional de Pesquisa e Desenvolvimento Tecnológico (CNPq) sobre as Atividades de Pesquisa Desenvolvidas no Primeiro Ano de Vigência da Bolsa de Estudos para Nível DCR-IF Referente ao Processo No. 304318/2003-5, *Report to the National Council of Scientific and Technological Development (CNPq)*, Recife, PE, Brazil, 37p, 2004. [available in the website www.edissonsavio.eng.br]

[39] E. S. G. Maciel, Relatório ao Conselho Nacional de Pesquisa e Desenvolvimento Tecnológico (CNPq) sobre as Atividades de Pesquisa Desenvolvidas no Segundo Ano de Vigência da Bolsa de Estudos para Nível DCR-IF Referente ao Processo No. 304318/2003-5, *Report to the National Council of Scientific and Technological Development (CNPq)*, Recife, PE, Brazil, 54p, 2005. [available in the website www.edissonsavio.eng.br]

[40] E. S. G. Maciel, and A. P. Pimenta, Thermochemical Non-Equilibrium Reentry Flows in Three-Dimensions – Part II – Unstructured Solutions, to be submitted to the *WSEAS TRANSACTIONS ON APPLIED AND THEORETICAL MECHANICS*, 2012.

[41] E. S. G. Maciel, and A. P. Pimenta, Reentry Flows in Chemical Non-Equilibrium in Three-Dimensions, *WSEAS TRANSACTIONS ON MATHEMATICS*, Vol. 11, Issue 3, March, 2012, pp. 262-282.

[42] S. K. Saxena, and M. T. Nair, An Improved Roe Scheme for Real Gas Flows, *AIAA Paper 2005-587*, 2005.

[43] Y. Liu, M. Vinokur, M. Panesi, and T. Magin, A Multi-Group Maximum Entropy Model for Thermo-Chemical Nonequilibrium, *AIAA Paper 2010-4332*.

[44] M. L. da Silva, V. Guerra, and J. Loureiro, State-Resolved Dissociation Rates for Extremely Nonequilibrium Atmospheric Entries, *J. Thermo. Phys.*, Vol. 21, No.1, 2007, pp. 40-49.

[45] S. C. Spiegel, D. L. Stefanski, H. Luo, and J. R. Edwards, A Cell-Centered Finite Volume Method for Chemically Reacting Flows on Hybrid Grids, *AIAA Paper 2010-1083*, 2010.

[46] B. Van Leer, Towards the Ultimate Conservative Difference Scheme. II. Monotonicity and Conservation Combined in a Second-Order Scheme, *Journal of Computational Physics*, Vol. 14, 1974, pp. 361-370.

[47] P. L. Roe, In *Proceedings of the AMS-SIAM Summer Seminar on Large-Scale Computation in Fluid Mechanics*, Edited by B. E. Engquist et al, *Lectures in Applied Mathematics*, Vol. 22, 1983, p. 163.